Monthly Notices
of the
ROYAL ASTRONOMICAL SOCIETY

MNRAS **432,** 530–553 (2013)
Advance Access publication 2013 April 11

doi:10.1093/mnras/stt490

Radiative efficiency, variability and Bondi accretion on to massive black holes: the transition from radio AGN to quasars in brightest cluster galaxies

H. R. Russell,[1]★ B. R. McNamara,[1,2,3] A. C. Edge,[4] M. T. Hogan,[4] R. A. Main[1] and A. N. Vantyghem[1]

[1]*Department of Physics and Astronomy, University of Waterloo, Waterloo, ON N2L 3G1, Canada*
[2]*Perimeter Institute for Theoretical Physics, Waterloo, ON N2L 2Y5, Canada*
[3]*Harvard–Smithsonian Center for Astrophysics, 60 Garden Street, Cambridge, MA 02138, USA*
[4]*Department of Physics, Durham University, Durham DH1 3LE, UK*

Accepted 2013 March 17. Received 2013 February 13; in original form 2012 November 6

ABSTRACT

We examine unresolved nuclear X-ray sources in 57 brightest cluster galaxies to study the relationship between nuclear X-ray emission and accretion on to supermassive black holes. The majority of the clusters in our sample have prominent X-ray cavities embedded in the surrounding hot atmospheres, which we use to estimate mean jet power and average accretion rate on to the supermassive black holes over the past several hundred Myr. We find that roughly half of the sample have detectable nuclear X-ray emission. The nuclear X-ray luminosity is correlated with average accretion rate determined using X-ray cavities, which is consistent with the hypothesis that nuclear X-ray emission traces ongoing accretion. The results imply that jets in systems that have experienced recent active galactic nucleus (AGN) outbursts, in the last $\sim 10^7$ yr, are 'on' at least half of the time. Nuclear X-ray sources become more luminous with respect to the mechanical jet power as the mean accretion rate rises. We show that nuclear radiation exceeds the jet power when the mean accretion rate rises above a few per cent of the Eddington rate, or a power output of $\sim 10^{45}$ erg s^{-1}, where the AGN apparently transitions to a quasar. The nuclear X-ray emission from three objects (A2052, Hydra A, M84) varies by factors of 2–10 on time-scales of 6 months to 10 years. If variability at this level is a common phenomenon, it can account for much of the scatter in the relationship between mean accretion rate and nuclear X-ray luminosity. We find no significant change in the spectral energy distribution as a function of luminosity in the variable objects. The nuclear X-ray luminosity is consistent with emission from either a jet, an advection-dominated accretion flow, or a combination of the two, although other origins are possible. We also consider the longstanding problem of whether jets are powered by the accretion of cold circumnuclear gas or nearly spherical inflows of hot keV gas. For a subset of 13 nearby systems in our sample, we re-examine the relationship between the jet power and the Bondi accretion rate. The results indicate weaker evidence for a trend between Bondi accretion and jet power, due to uncertainties in the cavity volumes and gas densities at the Bondi radius. We suggest that cold gas fuelling could be a likely source of accretion power in these objects; however, we cannot rule out Bondi accretion, which could play a significant role in low-power jets.

Key words: accretion, accretion discs – galaxies: active – galaxies: jets – X-rays: galaxies: clusters.

1 INTRODUCTION

Energetic feedback from supermassive black holes (SMBHs) plays an important role in the formation and evolution of galaxies. With this realization, the exploration and understanding of active galactic

★ E-mail: helen.russell@uwaterloo.ca

nuclei (AGN) has taken a new emphasis. Key lines of evidence include the relationship between nuclear black hole mass and the mass of the host galaxy ($M-\sigma$ relation; Magorrian et al. 1998; Kormendy & Gebhardt 2001; Merritt & Ferrarese 2001), which was likely imprinted through the quasar era ('quasar mode feedback'; Haehnelt, Natarajan & Rees 1998; Silk & Rees 1998; Di Matteo, Springel & Hernquist 2005), and the prevalence of radio bubbles in the X-ray atmospheres of giant elliptical and brightest cluster galaxies ('radio mode feedback'; Churazov et al. 2000; Fabian et al. 2000; McNamara et al. 2000; McNamara & Nulsen 2007). These forms of feedback are ultimately powered by binding energy released by accretion on to massive black holes. However, energy is released primarily in the form of radiation from quasars, while radio jets release their energy in a mechanical form.

Why black holes release their binding energy in different forms is poorly understood. Clues have come from the so-called Fundamental Plane of black holes (Merloni, Heinz & di Matteo 2003; Falcke, Körding & Markoff 2004). This relationship between the radio and X-ray power emerging from the vicinity of the black hole with black hole mass extends over nine orders of magnitude from stellar mass black holes to SMBHs. The continuity of this relationship indicates that the emergent properties of black holes are similar regardless of their mass. Furthermore, accreting black hole binaries undergo changes in emission states that seem to correlate with the accretion rate normalized to the black hole mass (e.g. Fender et al. 1999; Maccarone, Gallo & Fender 2003; Remillard & McClintock 2006).

Changes in the specific accretion rate apparently lead to structural changes in the accretion disc which govern the release of binding energy in the form of a jetted outflow or radiation. During periods of high accretion rate a geometrically thin and optically thick disc forms that dissipates its energy primarily in the form of radiation (Novikov & Thorne 1973; Shakura & Sunyaev 1973; Frank, King & Raine 2002). During periods of more modest accretion, a hot, radiatively inefficient accretion flow or advection-dominated accretion flow (ADAF) forms that releases its energy in the form of a jetted outflow or wind (e.g. Narayan & Yi 1994; Abramowicz et al. 1995; Narayan & McClintock 2008). ADAFs are geometrically thick, optically thin discs where the ion temperature substantially exceeds the electron temperature. In these discs, the inflow time-scale is much shorter than the cooling time-scale. Thus, the accretion energy cannot be radiated away and is either advected inwards with the flow or is released in a wind or radio jet (adiabatic inflow–outflow solutions, ADIOS; Blandford & Begelman 1999, 2004). In the context of SMBHs, a radiatively efficient disc is formed when the accretion rate approaches the Eddington value giving rise to a Seyfert nucleus or quasar. When the accretion rate falls below a few per cent of the Eddington rate, the nucleus becomes faint and a radio galaxy is formed (e.g. Churazov et al. 2005).

Galaxy formation models incorporating AGN feedback distinguish between radiatively dominated quasar feedback at early times and a mechanically dominated radio mode at late times (e.g. Springel, Di Matteo & Hernquist 2005; Bower et al. 2006; Croton et al. 2006; Hopkins et al. 2006; Sijacki & Springel 2006). Quasar feedback operates through intense radiation that is expected to couple to the gas and strong winds which drive gas from the host galaxy, quenching star formation and regulating the growth of the SMBH. This will eventually starve the SMBH of fuel and, as the accretion rate drops, a transition to mechanically dominated radio mode feedback is expected. The SMBH launches jets which regulate radiative cooling in the surrounding hot atmosphere and the growth of the most massive galaxies. The AGN activity is closely correlated with the properties of the host halo indicating that they form a feedback loop (e.g. Bîrzan et al. 2004; Dunn & Fabian 2004; Rafferty et al. 2006).

Despite evidence for rapid accretion on to their SMBHs, giant elliptical and brightest cluster galaxies (BCGs) in the nearby Universe rarely harbour quasars. The exceptions include H1821+643, 3C 186 and IRAS 09104+4109 (Crawford et al. 1999; Belsole et al. 2007; Russell et al. 2010; Siemiginowska et al. 2010, Cavagnolo et al. submitted). Instead, most harbour low-luminosity AGN, i.e. ADAFs (Fabian & Rees 1995; Di Matteo et al. 2000; Sambruna et al. 2000; Pellegrini 2005, 2010; Hlavacek-Larrondo & Fabian 2011). These low luminosities imply that their host galaxies harbour massive black holes exceeding $\sim 10^9\,\mathrm{M}_\odot$. Nuclear emission likely signals ongoing accretion. However, any dependence of the amplitude and form of the emission emerging from the nucleus on the accretion rate, as found in X-ray binaries, requires an independent means of estimating the accretion rate itself. Therefore, it is difficult to test nuclear emission models that predict a strong dependence on the form of nuclear power output with nuclear accretion rate (Falcke et al. 2004; Churazov et al. 2005). Here, we examine the nuclear emission properties in a sample of over 50 BCGs using the energy demands of X-ray cavities as a measure of mean nuclear accretion rate.

We assume $H_0 = 70\,\mathrm{km\,s^{-1}\ Mpc^{-1}}$, $\Omega_\mathrm{m} = 0.3$ and $\Omega_\Lambda = 0.7$. All errors are 1σ unless otherwise noted.

2 DATA REDUCTION AND ANALYSIS

2.1 Sample selection

We intend to explore the emergent properties of accreting black holes at the centres of clusters. Therefore, we have selected objects with large X-ray cavities which we use to estimate the mean accretion rate of each object over the past 10^7–10^8 yr. Sources with a range of cavity powers, and thus accretion rates, were selected. The sources were selected from cluster, group and elliptical galaxy samples which show evidence of AGN activity in the form of cavities in X-ray images (Bîrzan et al. 2004; Allen et al. 2006; Rafferty et al. 2006; Cavagnolo et al. 2010; O'Sullivan et al. 2011b). These objects were supplemented with other recently discovered X-ray point sources in cavity systems (RXC J0352.9+1941, RXC J1459.4−1811, RXC J1524.2−3154, RXC J1558.3−1410, Zw 348) and three non-cavity systems (Zw 2089, A2667, A611) each with a bright point source.

We have also included three quasars taken from the literature for comparison, H1821+643, IRAS 09104+4109 and 3C 186 (Siemiginowska et al. 2005, 2010; Russell et al. 2010; Cavagnolo et al. submitted). These sources have very different spectral energy distributions (SEDs) from the low-luminosity AGN dominating this sample. All three quasars have broad optical emission lines and bolometric luminosities of $\sim 10^{47}\,\mathrm{erg\,s^{-1}}$, far greater than the rest of the sample. Both H1821+643 and 3C 186 have strong big blue bumps in the optical–UV band whereas IRAS 09104+4109 is a heavily obscured quasar with most of its bolometric luminosity emerging in the infrared (IR). The big blue bump emission is usually interpreted as thermal emission from an accretion disc around the SMBH, which has then been re-radiated in the IR in IRAS 09104+4109. This component is absent in radiatively inefficient low-luminosity AGN (e.g. Chiaberge, Capetti & Macchetto 2005).

This sample is neither complete nor unbiased and we are mindful of this in our interpretation and analysis. Our sample overlaps the 15 objects analysed by Merloni & Heinz (2007) and we have quadrupled the sample size, including a large number of upper limits. In

total, 57 sources were selected covering a redshift range from the nearest Virgo ellipticals at a distance of only 17 Mpc to 3C 186 at $z = 1.06$ and a mass range from single elliptical galaxies to rich clusters. We sample mean accretion rates from 2×10^{-6} to $0.6\dot{M}_{\rm Edd}$ for the first time. The full list of sources, excluding the three quasars, is shown in Table 1.

2.2 *Chandra* data reduction

For each object in this sample, we selected the deepest *Chandra* observation in the archive for analysis (Table 1). Each observation was reprocessed using CIAO 4.4 and CALDB 4.4.7 provided by the *Chandra* X-ray Center. The level 1 event files were reprocessed to apply the latest gain and charge transfer inefficiency correction and then filtered to remove photons detected with bad grades. The improved background screening provided by VFAINT mode was also applied where available. Background light curves were extracted from the level 2 event files of neighbouring chips for observations on ACIS-I and from ACIS-S1 for observations on ACIS-S3. The background light curves were filtered using the LC_CLEAN script[1] provided by M. Markevitch to identify periods affected by flares. The final cleaned exposure times of each observation are detailed in Table 1. Standard blank-sky backgrounds were extracted for each observation, processed identically to the events file and reprojected to the corresponding sky position. The blank-sky background was then normalized to match the count rate in the 9.5–12 keV energy band in the observed data set. This correction was less than 10 per cent for the majority of the observations. Each normalized blank-sky background was also checked against the observed background spectrum extracted from a source-free region of each data set to ensure it was a good match.

2.3 X-ray point source flux

Fig. 1 shows an example of a clear detection of surface brightness depressions indicating cavities and an X-ray point source at the centre of A2052 (Blanton et al. 2011). We required at least a 3σ detection above the background, where the background error considers only Poisson statistics, in a hard 3–7 keV energy band image to confirm the detection of an X-ray point source. The majority of the sources were not detected with sufficient counts above the cluster background to generate a reasonable spectrum. Therefore, we used two alternative methods, based on those described by Hlavacek-Larrondo & Fabian (2011), to calculate the X-ray flux of the confirmed sources and 1σ upper limits on the non-detections. Note that all point source fluxes and luminosities given are corrected for Galactic and intrinsic absorption.

The photometric method sums the point source flux in a 1 arcsec radius region using an exposure-corrected image, which was weighted by a spectral model for the point source. This region was centred on the peak in the X-ray cluster emission if no point source was detected. The only exception was the Centaurus cluster where we used the position of the radio source as the centre (Taylor et al. 2006). For the majority of the sample, we used an absorbed power-law model PHABS(ZPHABS(POWERLAW)) with no intrinsic absorption, a photon index $\Gamma = 1.9$ (e.g. Gilli, Comastri & Hasinger 2007) and Galactic absorption from Kalberla et al. (2005). For sources detected with several hundred source counts or more, this model was fitted to an extracted spectrum using XSPEC version 12 (Arnaud 1996) with the intrinsic absorption and the photon index left free. These model parameters are detailed in Table 1. We used the modified version of the C-statistic available in XSPEC to determine the best-fitting parameters for spectra with a low number of counts (Cash 1979; Wachter, Leach & Kellogg 1979). Note that the intrinsic absorption was set to zero for sources with only upper limits and the photon index was set to 1.9 where this was consistent with the best-fitting value within the error. The cluster background was subtracted using an annulus around the point source from 1.5 to 2.5 arcsec and an exposure-corrected image that was uniformly weighted at the average peak in the cluster spectrum around 1.5 keV. The point source flux was also corrected for the fraction of the point spread function (PSF) falling in the 1 arcsec region (90 per cent[2]). A larger region encompassing more of the PSF also included a greater fraction of cluster background, which increased the measurement uncertainty.

However, for galaxy clusters and groups with steep central surface brightness peaks this method is likely to significantly undersubtract the background cluster emission. We therefore also employed a spectroscopic method where we fit a spectrum extracted from the 1 arcsec radius point source region with a model for both the point source and cluster emission. The parameters for the cluster model were determined by extrapolating profiles of the projected cluster properties in to the point source region. These profiles were generated by extracting spectra from a series of circular annuli centred on the point source and fitting them with a suitable spectral model to determine the temperature, metallicity and normalization. We required a minimum of ∼2000 source counts per region to ensure good constraints on the cluster parameters. However, fewer counts per region were allowed for the low-temperature sources in the sample where the Fe L line emission improves temperature diagnostics. Point sources were identified using the CIAO algorithm WAVDETECT, visually confirmed and excluded from the analysis (Freeman et al. 2002). Regions of non-thermal jet emission were also excluded. The cluster spectra were grouped to contain a minimum of 20 counts per spectral channel, restricted to the energy range 0.5–7 keV and fit in XSPEC with appropriate responses, ancillary responses and blank-sky backgrounds.

For the majority of the clusters, an absorbed single temperature PHABS(MEKAL) model (Mewe, Gronenschild & van den Oord 1985; Mewe, Lemen & van den Oord 1986; Balucinska-Church & McCammon 1992; Kaastra 1992; Liedahl, Osterheld & Goldstein 1995) provided a good fit to the cluster emission in each annulus. This model was insufficient for some of the bright, nearby clusters with multiphase gas signatures, such as Centaurus, M87 and A2052. In these cases, a second MEKAL component or a MKCFLOW component was added to the spectral model. The cluster redshift and Galactic column density were fixed to the values given in Table 1. Abundances were measured assuming the abundance ratios of Anders & Grevesse (1989). For the multitemperature models, the metallicity was tied between the two components and, for the MKCFLOW model, the lower temperature was fixed to 0.1 keV and the higher temperature was tied to that of MEKAL component. We produced radial profiles for the best-fitting temperature, metallicity and normalization parameters and used power-law fits to the inner points to extrapolate these properties into the point source region. The cluster spectra were also used to determine the Galactic absorption for sources located on regions of the sky where the absorption is highly variable. The spectral fits were repeated for annuli at large radii, excluding cooler gas components in the cluster core, leaving

[1] See http://cxc.harvard.edu/contrib/maxim/acisbg/.

[2] http://cxc.harvard.edu/proposer/POG

Table 1. Sample properties and point source fluxes.

Target	Redshift	Obs. ID	Aimpoint	Exposure[a] (ks)	$n_{\rm H}$[b] (10^{22} cm^{-2})	$n_{\rm H,\,z}$ (10^{22} cm^{-2})	Γ	$F_{\rm P,2-10\,keV}$[c] (10^{-14} erg cm^{-2} s^{-1})	$F_{\rm S,2-10\,keV}$[c] (10^{-14} erg cm^{-2} s^{-1})	References
2A0335+096	0.0349	7939	S3	49.5	0.2218*	0	1.9	<2.3	<0.1	[1]
3C 295	0.4641	2254	I3	75.6	0.0134	43^{+6}_{-5}	1.9	76 ± 4	55 ± 3	[2],[3]
3C 388	0.0917	5295	I3	26.3	0.0555	0	1.9	4.0 ± 0.3	2 ± 1	[4],[1]
3C 401	0.2011	4370	S3	22.7	0.0582	0	1.9	3.7 ± 0.3	3.7 ± 0.3	[2],[1]
4C 55.16	0.2412	4940	S3	64.5	0.0429	0	$1.55^{+0.09}_{-0.08}$	7.3 ± 0.3	$6.9^{+0.3}_{-0.5}$	[5],[1]
A85	0.0551	904	I0	38.2	0.0278	0	1.9	<2.2	<2.1	[1]
A133	0.0566	9897	I3	67.9	0.0159	0	1.9	<0.8	<0.2	[1]
A262	0.0166	7921	S3	108.6	0.0567	0	1.9	<0.49	<0.04	[1]
A478	0.0881	1669	S3	39.3	0.2778*	0	1.9	<3.2	<1.4	[6],[1]
A611	0.2880	3194	S3	32.0	0.0447	0	1.9	3.0 ± 0.2	$3.1^{+0.2}_{-0.8}$	–
A1795	0.0625	10 900	S3	15.8	0.0119	0	1.9	<1.8	<1.6	[1]
A1835	0.2523	6880	I3	109.2	0.0204	0	1.9	<3.1	<1.2	[6],[1]
A2029	0.0773	4977	S3	74.7	0.0325	0	1.9	<4.5	<1.4	[1]
A2052	0.0351	5807	S3	123.8	0.0272	0	1.9	3.8 ± 0.1	$3.1^{+0.2}_{-0.3}$	[7],[1]
A2199	0.0302	10 748	I3	40.6	0.0089	0	1.9	3.1 ± 0.3	0.9 ± 0.6	[8],[1]
A2390	0.2280	4193	S3	70.6	0.0768*	0	1.9	1.4 ± 0.1	$1.0^{+0.1}_{-0.2}$	–
A2597	0.0852	7329	S3	56.3	0.0248	0	1.9	<2.3	<1.3	[1]
A2667	0.2300	2214	S3	8.4	0.0173	0	1.9	2.4 ± 0.4	2.8 ± 0.4	–
A4059	0.0475	5785	S3	85.9	0.0121	0	1.9	<0.72	<0.08	[1]
Centaurus	0.0114	4954	S3	87.2	0.0948*	0	1.9	<1.6	<0.10	[6],[1]
Cygnus A	0.0561	1707	S3	9.2	0.272	19.6 ± 0.7	1.9	3160 ± 70	2560 ± 60	[6],[1]
HCG62	0.0137	10 462	S3	65.1	0.0332	0	1.9	<0.67	<0.03	[1]
Hercules A	0.1540	6257	S3	48.5	0.0618	0	1.9	<0.94	<0.53	[1]
Hydra A	0.0549	4970	S3	94.6	0.0468	3.5 ± 0.3	1.9	24 ± 1	$14.5^{+0.8}_{-0.7}$	[9],[1]
M84	0.0035	5908	S3	45.1	0.0299	$0.12^{+0.03}_{-0.02}$	2.13 ± 0.09	17.5 ± 0.4	15^{+1}_{-3}	[10],[1]
M87	0.0044	1808	S3	12.8	0.0194	0.06 ± 0.01	2.37 ± 0.07	67 ± 1	66 ± 4	[11],[1]
M89	0.0011	2072	S3	53.4	0.0262	0.09 ± 0.03	2.3 ± 0.1	5.5 ± 0.2	3 ± 2	[12],[13]
MKW3S	0.0450	900	I3	51.9	0.0268	0	1.9	<1.0	<0.2	[1]
MS 0735.6+7421	0.2160	10 470	I3	133.8	0.0328	0	1.9	<0.95	<0.12	[14]
NGC 507	0.0165	2882	I3	40.0	0.0525	0	1.9	<1.1	<0.1	[15]
NGC 1316	0.0059	2022	S3	20.2	0.0240	0	1.9	<3.0	<2.2	[15]
NGC 1600	0.0156	4283	S3	20.5	0.0349	0	1.9	<0.6	<0.2	[15]
NGC 4261	0.0075	9569	S3	99.9	0.0175	$3.0^{+0.6}_{-0.5}$	0.9 ± 0.2	126 ± 2	74 ± 2	[16],[17]
NGC 4472	0.0033	11 274	S3	39.7	0.0153	0	1.9	<2.4	<0.1	[15]
NGC 4636	0.0031	3926	I3	67.8	0.0190	0	1.9	<0.9	<0.3	[15]
NGC 4782	0.0154	3220	S3	49.3	0.0337	0	1.9	0.84 ± 0.09	0.7 ± 0.1	[18],[15]
NGC 5044	0.0093	9399	S3	82.5	0.0487	$0.23^{+0.08}_{-0.07}$	1.9	2.6 ± 0.2	$1.4^{+0.4}_{-0.3}$	[19],[15]
NGC 5813	0.0066	9517	S3	98.8	0.0918*	0	1.9	<1.02	<0.3	[20]
NGC 5846	0.0057	7923	I3	84.7	0.0429	0	1.9	<0.72	<0.05	[15]
NGC 6269	0.0348	4972	I3	35.3	0.0510	0	1.9	<2.4	<0.08	[15]
NGC 6338	0.0274	4194	I3	44.5	0.0223	0	1.9	<2.2	<1.4	[15]
PKS 0745−191	0.1028	12 881	S3	116.0	0.38	0	1.9	4.8 ± 0.3	$2.6^{+0.2}_{-0.4}$	[1]
PKS 1404−267	0.0230	12 884	S3	83.5	0.0578*	0.04 ± 0.02	2.01 ± 0.06	21.4 ± 0.4	19.8 ± 0.7	[21],[1]
RBS 797	0.3540	7902	S3	38.3	0.0228	$3.8^{+0.9}_{-0.8}$	1.4 ± 0.2	61 ± 2	41 ± 2	[22]
RXC J0352.9+1941	0.1090	10 466	S3	27.2	0.1440*	3.6 ± 0.4	1.9	36 ± 2	32 ± 2	–
RXC J1459.4−1811	0.2357	9428	S3	39.5	0.0736	$5.4^{+1.0}_{-0.8}$	1.9	21 ± 1	13 ± 1	–
RXC J1524.2−3154	0.1028	9401	S3	40.9	0.1107*	0.5 ± 0.2	1.9	5.7 ± 0.5	3.2 ± 0.4	–
RXC J1558.3−1410	0.0970	9402	S3	36.0	0.1060	15^{+5}_{-3}	1.9	41 ± 3	22 ± 2	–
Sérsic 159-03	0.0580	11 758	I3	93.3	0.0114	0	1.9	<1.0	<0.07	[1]
UGC 408	0.0147	11 389	S3	93.8	0.0256	$0.23^{+0.06}_{-0.05}$	2.2 ± 0.2	3.3 ± 0.1	2.8 ± 0.2	[20]
Zw 348	0.2535	10 465	S3	48.9	0.0250	$0.8^{+0.7}_{-0.4}$	1.9	4.4 ± 0.4	2.9 ± 0.4	–
Zw 2089	0.2350	10 463	S3	38.6	0.0286	22 ± 2	1.9	203 ± 7	127^{+6}_{-5}	–
Zw 2701	0.2150	12 903	S3	95.8	0.0075	0	1.9	<0.53	<0.3	[6],[23]
Zw 3146	0.2906	9371	I3	34.5	0.0246	0	1.9	<5.0	<3.3	[6],[1]

Note. [a]Final cleaned exposure times. [b]Column densities marked with asterisks '*' were found to be higher than the Galactic value measured by Kalberla et al. (2005) (see Section 2.3). [c]Unabsorbed flux with 1σ errors and upper limits on the photometric $F_{\rm P,2-10\,keV}$ and spectroscopic $F_{\rm S,2-10\,keV}$ values. References: [1] Rafferty et al. (2006), [2] Hardcastle, Evans & Croston (2006), [3] Hlavacek-Larrondo et al. (2012), [4] Evans et al. (2006), [5] Hlavacek-Larrondo et al. (2011), [6] Hlavacek-Larrondo & Fabian (2011), [7] Blanton, Sarazin & McNamara (2003), [8] Di Matteo et al. (2001), [9] McNamara et al. (2000), [10] Balmaverde, Capetti & Grandi (2006), [11] Di Matteo et al. (2003), [12] Machacek et al. (2006), [13] Allen et al. (2006), [14] Vantyghem et al., in preparation, [15] Cavagnolo et al. (2010), [16] Chiaberge et al. (2003a), [17] O'Sullivan et al. (2011), [18] Machacek et al. (2007), [19] David et al. (2009), [20] O'Sullivan et al. (2011b), [21] Johnstone et al. (2005), [22] Cavagnolo et al. (2011), [23] Ma et al., in preparation.

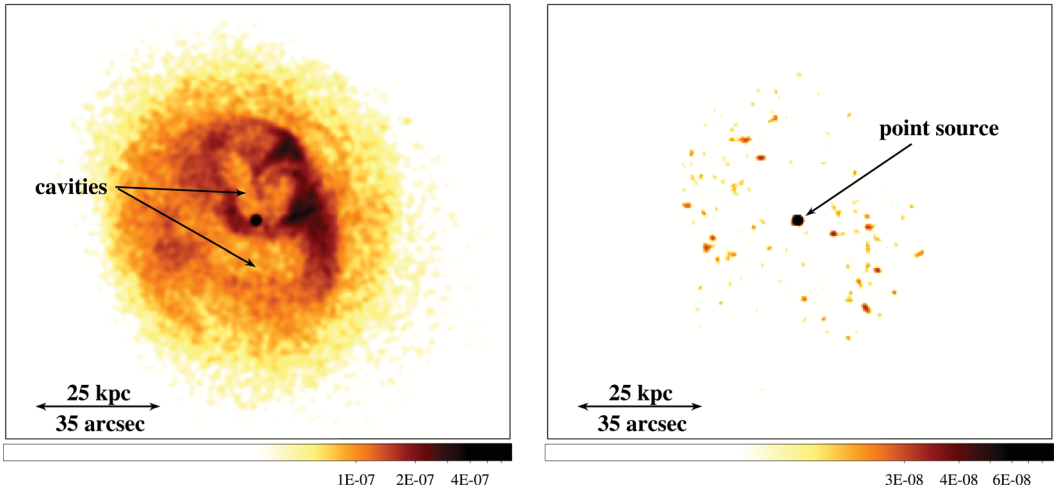

Figure 1. Exposure-corrected *Chandra* images covering the same field of Abell 2052 (see Blanton et al. 2011). The colour bar has units photons cm^{-2} s^{-1} $pixel^{-1}$. Left: 0.5–7 keV energy band showing the X-ray cavities. Right: 3–7 keV energy band showing the AGN point source detection.

the n_H parameter free (Table 1). The central cluster parameters are given in Table 2.

The spectrum extracted from the point source region was then fitted with a combined model for both the point source and cluster emission plus the appropriate blank-sky background. The similarity between the power-law and thermal model components, particularly for higher temperature clusters, can make it difficult to distinguish them with *Chandra*'s spectral resolution. Most of the model parameters were therefore constrained for the fit. The parameters for the point source model were set to those detailed in Table 1 with only the normalization left free. The cluster model temperature was fixed to the value determined by extrapolating from neighbouring annuli. The metallicity was fixed to the value in the neighbouring cluster annulus as it was generally not found to vary significantly at these small radii. The normalization of the cluster component was problematic because it was strongly affected by cavity substructure in the core, which produced large variation. We therefore constrained the cluster normalization in the point source region to be no less than the normalization from the neighbouring annulus, scaled by the ratio of their respective areas. The XSPEC CFLUX model was used to determine the flux or an upper limit for the unabsorbed point source component (Table 1).

The main source of error in both the photometric and spectroscopic measurements of the point source flux is the subtraction of the cluster emission. The photometric method is likely to underestimate the background cluster emission and should therefore be treated as an upper limit on the point source flux. The spectroscopic method improves on this by allowing for the increase in cluster surface brightness towards the cluster centre but may significantly overestimate the cluster background because it is indistinguishable from the power-law component. For strongly obscured point sources and low-temperature cluster emission, the spectroscopic method is likely to be a significant improvement over the photometric method. For higher temperature clusters, the photometric method may be more accurate. We have therefore listed both the photometric and spectroscopic fluxes in Table 1 but used the generally more accurate spectroscopic flux in our analysis. The possible bias in this measurement for higher temperature clusters with strong 3–7 keV emission is discussed in Section 3.2.

Several of the brighter point sources in the sample were significantly piled up in the longest *Chandra* exposures initially selected for analysis. Pile up occurs whenever two or more photons, arriving in the same detector region and within a single ACIS frame integration time, are detected as a single event (Davis 2001). For M87 and Cygnus A, there were alternative observations available in the archive with shorter 0.4 s frame times for which the point source was not piled up. These short frame time observations were used to calculate the point source flux. The cluster background was analysed using the deeper exposures but the piled-up regions were excluded. All the archival observations of the point source in Perseus, where the cluster centre is not positioned far off-axis distorting the PSF, were found to be significantly piled up. Perseus was therefore excluded from this sample.

Fig. 2 compares our spectroscopic point source fluxes with measurements for the same sources available in the literature. The majority of the fluxes are consistent within the errors. Small variations are expected due to differences in background subtraction and the position selected for the upper limits but there are three sources, Centaurus, NGC 4782 and RBS 797, with significantly different values which we have considered in detail. There is only a modest discrepancy for RBS 797 given the large errors and this is likely due to the additional model components used for the Cavagnolo et al. (2011) result. The differences for Centaurus and NGC 4782 are due to our use of a two temperature rather than a single-temperature cluster model. The best-fitting single temperature falls mid-way between the preferred higher and lower temperature values of the two-component model and therefore significantly underestimates the cluster surface brightness in the 2–10 keV band used to determine the point source flux. Our two-component model therefore finds a higher cluster background and a significantly lower nuclear point source upper limit.

2.4 Cavity power

The cavities observed in the X-ray images of this sample allow a direct measurement of the mechanical output from the AGN (Bîrzan et al. 2004; Churazov et al. 2000; Dunn & Fabian 2004; McNamara & Nulsen 2007). For a bubble filled with relativistic plasma, the energy required to inflate it is given by $E = 4PV$, where the bubble is assumed to be in pressure equilibrium with the surrounding intracluster medium (ICM). The bubble energy is then divided by the sound speed time-scale or the buoyant rise time to estimate the

Table 2. Cluster centre parameters for the spectroscopic method calculating point source flux.

Target	Temperature (keV)	Metallicity ($Z_\odot$)	Normalization (cm^{-5})	$\dot{M}$ ($M_\odot\ yr^{-1}$)	Target	Temperature (keV)	Metallicity ($Z_\odot$)	Normalization (cm^{-5})	$\dot{M}$ ($M_\odot\ yr^{-1}$)
2A0335	$1.8^{+0.2}_{-0.1}$	$0.7^{+0.2}_{-0.1}$	$1.1 \pm 0.3 \times 10^{-5}$	0.19 ± 0.01	MS0735	3.1 ± 0.2	0.7 ± 0.1	$1.29 \pm 0.05 \times 10^{-5}$	
3C 295	2.6 ± 0.3	0.5 ± 0.1	$1.08 \pm 0.04 \times 10^{-5}$		NGC 507	0.77 ± 0.04	0.32 ± 0.04	$7.9 \pm 0.6 \times 10^{-7}$	
3C 388	3.4 ± 0.1	1.1 ± 0.2	$4.6 \pm 0.2 \times 10^{-7}$		NGC 1316	0.68 ± 0.01	0.19 ± 0.02	$2.5 \pm 0.2 \times 10^{-6}$	
4C55.16	$2.1^{+0.2}_{-0.1}$	0.8 ± 0.1	$1.71 \pm 0.09 \times 10^{-5}$		NGC 1600	$0.99^{+0.03}_{-0.02}$	$0.27^{+0.05}_{-0.04}$	$5.2 \pm 0.5 \times 10^{-7}$	
A85	3.1 ± 0.3	1.0 ± 0.2	$8.9 \pm 0.5 \times 10^{-6}$		NGC 4261	0.55 ± 0.01	$0.37^{+0.06}_{-0.05}$	$1.5 \pm 0.2 \times 10^{-5}$	
A133	1.8 ± 0.1	1.1 ± 0.2	$7.7 \pm 0.6 \times 10^{-6}$		NGC 4472	0.63 ± 0.01	$1.3^{+0.6}_{-0.3}$	$3 \pm 1 \times 10^{-6}$	
A262	3.6 ± 0.4	$2.5^{+0.7}_{-0.5}$	$<3.4 \times 10^{-7}$	$9.0 \pm 0.4 \times 10^{-3}$		2.4 ± 0.5	$1.3^{+0.6}_{-0.3}$	$1.4 \pm 0.3 \times 10^{-6}$	
A478	2.7 ± 0.2	0.7 ± 0.1	$4.6 \pm 0.2 \times 10^{-5}$		NGC 4636	0.43 ± 0.01	0.30 ± 0.05	$9 \pm 1 \times 10^{-6}$	
A611	6 ± 1	0.5 ± 0.2	$3.8 \pm 0.1 \times 10^{-6}$		NGC 4782	$0.37^{+0.09}_{-0.07}$	$0.6^{+0.4}_{-0.2}$	$4 \pm 2 \times 10^{-8}$	
A1795	$3.1^{+0.4}_{-0.3}$	0.6 ± 0.1	$1.53 \pm 0.07 \times 10^{-5}$			$2.2^{+1.2}_{-0.9}$	$0.6^{+0.4}_{-0.2}$	$1.3 \pm 0.2 \times 10^{-7}$	
A1835	$3.4^{+0.3}_{-0.2}$	0.42 ± 0.08	$6.4 \pm 0.2 \times 10^{-5}$		NGC 5044	0.60 ± 0.02	$0.32^{+0.08}_{-0.06}$	$6 \pm 1 \times 10^{-6}$	
A2029	2.9 ± 0.1	1.8 ± 0.2	$4.7 \pm 0.2 \times 10^{-5}$			$1.9^{+1.0}_{-0.6}$	$0.32^{+0.08}_{-0.06}$	$1.2 \pm 0.4 \times 10^{-6}$	
A2052	$2.8^{+0.4}_{-0.3}$	$2.5^{+0.7}_{-0.5}$	$<1.4 \times 10^{-6}$	0.02 ± 0.001	NGC 5813	0.61 ± 0.01	0.30 ± 0.05	$7.1 \pm 0.6 \times 10^{-6}$	
A2199	1.9 ± 0.2	0.7 ± 0.2	$2.6 \pm 0.3 \times 10^{-5}$		NGC 5846*	0.59 ± 0.01	$0.44^{+0.12}_{-0.09}$	$2.2 \pm 0.5 \times 10^{-6}$	
A2390	3.1 ± 0.3	0.7 ± 0.1	$2.03 \pm 0.07 \times 10^{-5}$			1.5	$0.44^{+0.12}_{-0.09}$	$9.4 \pm 0.9 \times 10^{-7}$	
A2597	1.9 ± 0.1	0.30 ± 0.08	$3.1 \pm 0.1 \times 10^{-5}$		NGC 6269	$1.4^{+0.3}_{-0.2}$	$0.7^{+0.2}_{-0.1}$	$3.2 \pm 0.3 \times 10^{-7}$	
A2667	$1.6^{+0.4}_{-0.3}$	0.5 ± 0.1	$1.19 \pm 0.05 \times 10^{-5}$		NGC 6338	1.66 ± 0.09	2 ± 1	$2.1 \pm 0.7 \times 10^{-6}$	
A4059	$2.0^{+0.4}_{-0.3}$	$1.9^{+0.5}_{-0.4}$	$2.2 \pm 0.4 \times 10^{-6}$	0.031 ± 0.003		0.80 ± 0.04	2 ± 1	$4 \pm 2 \times 10^{-7}$	
Centaurus	$1.36^{+0.07}_{-0.06}$	$1.1^{+0.4}_{-0.3}$	$7 \pm 1 \times 10^{-6}$		PKS 0745	3.6 ± 0.1	$0.56^{+0.09}_{-0.08}$	$6.5 \pm 0.2 \times 10^{-5}$	
	0.54 ± 0.01	$1.1^{+0.4}_{-0.3}$	$4 \pm 1 \times 10^{-6}$		PKS 1404	0.62 ± 0.04	$0.9^{+0.3}_{-0.2}$	$5 \pm 1 \times 10^{-7}$	
Cygnus A	5.0 ± 0.6	2.0 ± 0.4	$9.6 \pm 0.7 \times 10^{-6}$			1.7 ± 0.1	$0.9^{+0.3}_{-0.2}$	$2.1 \pm 0.3 \times 10^{-6}$	
HCG62	$1.8^{+0.6}_{-0.5}$	$1.0^{+0.5}_{-0.3}$	$4.2 \pm 0.7 \times 10^{-7}$		RXC J0352	$0.95^{+0.07}_{-0.06}$	0.30 ± 0.05	$2.1 \pm 0.1 \times 10^{-5}$	
	$0.59^{+0.02}_{-0.01}$	$1.0^{+0.5}_{-0.3}$	$1.3 \pm 0.5 \times 10^{-6}$		RXC J1459	4.0 ± 0.2	$0.8^{+0.2}_{-0.1}$	$1.81 \pm 0.08 \times 10^{-5}$	
Hercules A	1.4 ± 0.1	0.7 ± 0.1	$7.1 \pm 0.4 \times 10^{-6}$		RXC J1524	2.23 ± 0.08	$0.60^{+0.11}_{-0.09}$	$3.9 \pm 0.2 \times 10^{-5}$	
Hydra A	3.4 ± 0.2	$0.62^{+0.10}_{-0.09}$	$1.9 \pm 0.1 \times 10^{-5}$	0.06 ± 0.01	RXC J1558	3.0 ± 0.3	1.2 ± 0.2	$8.8 \pm 0.5 \times 10^{-6}$	
M84*	0.52 ± 0.02	0.3	$3.08 \pm 0.09 \times 10^{-6}$		Sérsic 159	1.65 ± 0.08	$0.34^{+0.07}_{-0.06}$	$1.54 \pm 0.09 \times 10^{-5}$	
	3.0	0.3	$1.2 \pm 0.1 \times 10^{-6}$		UGC 408	$0.9^{+0.2}_{-0.1}$	0.20 ± 0.05	$1.9 \pm 0.2 \times 10^{-7}$	
M87	5^{+3}_{-2}	$1.3^{+0.5}_{-0.3}$	$7 \pm 1 \times 10^{-6}$	$3.2 \pm 0.6 \times 10^{-4}$	Zw 2089	2.6 ± 0.2	0.6 ± 0.1	$2.8 \pm 0.2 \times 10^{-5}$	
M89*	0.84 ± 0.03	0.3	$2.51 \pm 0.08 \times 10^{-6}$		Zw 2701	$3.2^{+0.4}_{-0.3}$	1.3 ± 0.2	$6.6 \pm 0.3 \times 10^{-6}$	
	3.0	0.3	$8.4 \pm 0.9 \times 10^{-7}$		Zw 3146	2.4 ± 0.2	0.5 ± 0.1	$4.4 \pm 0.2 \times 10^{-5}$	
MKW3S	3.3 ± 0.3	0.9 ± 0.2	$5.6 \pm 0.3 \times 10^{-6}$						

Note. *M84, M89 and NGC 5846 have a fixed hard X-ray component (Finoguenov & Jones 2001; Finoguenov et al. 2008; Machacek et al. 2006, 2011).

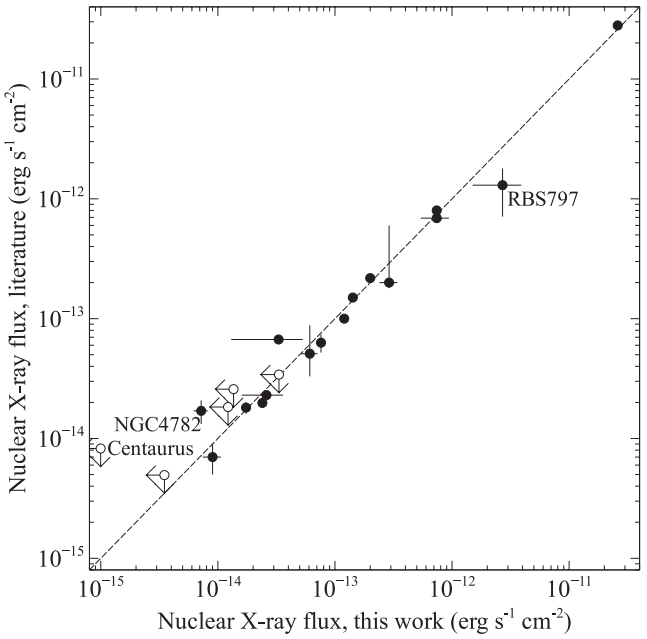

Figure 2. Comparison of the spectroscopic point source fluxes with values from the literature (see Table 1). Note that the point source fluxes shown here were evaluated in the same energy band as those given in the literature and may differ significantly from those in Table 1.

power input to the ICM (see e.g. Bîrzan et al. 2004). Cavity powers for the majority of the targets in this sample were available in the literature and otherwise estimated following Bîrzan et al. (2004) (see Table 1). These values should be treated generally as lower limits on the total mechanical energy input by the central AGN. The data sets available in the *Chandra* archive for this cluster sample vary from snapshot 10 ks exposures to almost complete orbit exposures over 100 ks. Even for the nearest and brightest galaxy clusters, deeper exposures continue to discover new cavities (e.g. Fabian et al. 2011). Some cavities will therefore have been missed from these estimates of the total power. In addition, weak shocks and sound waves have also been found to contribute significantly to the power output of the central AGN (e.g. Fabian et al. 2003, 2006; Forman et al. 2005).

Estimates of the cavity power can be complicated by the presence of significant X-ray emission from jets. For example, the synchrotron self-Compton emission in the centre of 3C 295 makes it difficult to determine the extent of the inner cavities and therefore the total power is significantly underestimated for this system (Harris et al. 2000; Allen, Ettori & Fabian 2001). The cavity power estimate for 3C 295 is therefore shown as a lower limit. Three sources in our sample, Zw 2089, A611 and A2667, have point sources but no detected cavities in the X-ray images. Ideally, these sources would be included in the analysis with upper limits on the cavity power. However, it is difficult to place meaningful constraints on the possible size of non-detected cavities, particularly at large radius where the noise increases and the X-ray surface brightness drops off rapidly (see Bîrzan et al. 2012). These sources have therefore been included with only illustrative upper limits, not quantitative.

By comparing the radiative output from the X-ray point source with the cavity power, we can calculate the radiative efficiency of the AGN. The total power output from the AGN can also be used to infer a mean accretion rate, given an assumption of the accretion efficiency. We refer throughout to a mean rather than instantaneous accretion rate as this method estimates the average accretion requirements over the $\sim 10^7$ yr age of each cavity. We have also calculated the theoretical Eddington and Bondi accretion rates for comparison with the inferred accretion rates for the sample.

2.5 Eddington luminosity

The Eddington luminosity indicates the limiting luminosity of the SMBH when the outward pressure of radiation prevents the gravitational infall of accreting material. For a fully ionized plasma, the Eddington luminosity can be expressed as

$$\frac{L_{\rm Edd}}{\rm erg\ s^{-1}} = 1.26 \times 10^{47} \left(\frac{M_{\rm BH}}{10^9\ {\rm M}_\odot} \right), \quad (1)$$

where $M_{\rm BH}$ is the SMBH mass. Dynamical estimates of the black hole mass were used where these were available (Cygnus A, Tadhunter et al. 2003; Rafferty et al. 2006; M84, Walsh, Barth & Sarzi 2010; M87, Gebhardt et al. 2011; NGC 4261, Ferrarese, Ford & Jaffe 1996). For the majority of the sample without dynamical masses, we relied on well-studied relations between the black hole mass and the properties of the host galaxy. Following Graham (2007), the apparent *K*-band magnitude of the host galaxy from the 2MASS catalogue[3] (Skrutskie et al. 2006) was converted to an absolute magnitude, corrected for Galactic extinction (Schlegel, Finkbeiner & Davis 1998), redshift and evolution (Poggianti 1997), and used to estimate the black hole mass. 3C 401, RBS 797 and Zw 348 have detected X-ray point sources but no available apparent *K*-band magnitudes for this analysis and are not included in plots with Eddington accretion rate or luminosity scaling. Dalla Bontà et al. (2009) find an upper limit on the central black hole mass in A2052 from dynamical measurements, which is consistent with the value calculated from the apparent *K*-band magnitude. The black hole masses for this sample are given in Table 3.

There are however potential problems with the use of *K*-band magnitudes to estimate black hole masses. Lauer et al. (2007) suggest that the apparent magnitudes from 2MASS are not deep enough to capture the extent of the BCG envelope and therefore will underestimate the total luminosity and black hole mass. Batcheldor et al. (2007) instead suggest that the BCG extended envelope, formed of debris from tidal stripping, is unlikely to be closely associated with the central galaxy dynamics. We have therefore considered these black hole masses to be estimates and, where possible, present the results with and without scaling by the Eddington accretion rate.

2.6 Bondi accretion rate

The primary aim of this paper is to examine the relationship between accretion and power output in SMBHs. One of the outstanding problems is whether the jets are powered by cold accretion from circumnuclear accretion discs of atomic and molecular gas or whether they are fuelled by a nearly spherical inflow of hot keV gas. It is impossible to prove either case because we lack imaging on the scale of and below the Bondi radius for almost all objects in our sample. However, this has been done in nearby ellipticals where *Chandra*'s resolution is close to the size of the Bondi sphere (e.g. Di Matteo et al. 2001, 2003; Churazov et al. 2002; Pellegrini et al. 2003). This problem has been addressed by Allen et al. (2006) in a sample of nearby ellipticals and by Rafferty et al. (2006) in a more distant sample with properties similar to our own and these studies

[3] http://www.ipac.caltech.edu/2mass

Table 3. Black hole masses and mean accretion rates scaled by the Eddington rate. Dynamical masses were available for Cygnus A (Tadhunter et al. 2003; Rafferty et al. 2006), M84 (Walsh et al. 2010), M87 (Gebhardt et al. 2011) and NGC 4261 (Ferrarese et al. 1996). $M_{\rm BH,\,dyn}$ or $M_{\rm BH,L_K}$ were used for all the analysis except for the Bondi accretion parameters where $M_{\rm BH,\,dyn}$ or $M_{\rm BH,\,\sigma}$ were used to ensure consistency with Allen et al. (2006). No values were available for 3C 401, RBS 797 and Zw 348 so these objects are not included.

Target	$M_{\rm BH,\,dyn}$ ($10^9\,M_\odot$)	$M_{\rm BH,\,\sigma}$ ($10^9\,M_\odot$)	$M_{\rm BH,L_K}$ ($10^9\,M_\odot$)	$\dot{M}/\dot{M}_{\rm Edd}$	Target	$M_{\rm BH}$ ($10^9\,M_\odot$)	$M_{\rm BH,\,\sigma}$ ($10^9\,M_\odot$)	$M_{\rm BH,L_K}$ ($10^9\,M_\odot$)	$\dot{M}/\dot{M}_{\rm Edd}$
2A0335			1.2 ± 0.3	$1.6^{+1.5}_{-0.6} \times 10^{-4}$	MKW3S			0.7 ± 0.2	$0.004^{+0.005}_{-0.001}$
3C 295			5 ± 2	0.004 ± 0.002	MS0735			1.5 ± 0.5	0.03 ± 0.01
3C 388			1.3 ± 0.4	$0.0012^{+0.0018}_{-0.0006}$	NGC 507		0.7 ± 0.1	1.0 ± 0.3	$1.6^{+0.5}_{-0.7} \times 10^{-4}$
4C55.16			1.2 ± 0.3	$0.003^{+0.003}_{-0.001}$	NGC 1316		0.28 ± 0.04	1.5 ± 0.4	$6^{+2}_{-3} \times 10^{-6}$
A85			2.0 ± 0.6	$1.5^{+1.6}_{-0.7} \times 10^{-4}$	NGC 1600			1.1 ± 0.3	$1.3 \pm 0.7 \times 10^{-5}$
A133			1.4 ± 0.4	$0.003^{+0.002}_{-0.001}$	NGC 4261	0.6 ± 0.1			$1.5 \pm 0.8 \times 10^{-4}$
A262			0.8 ± 0.2	$9^{+8}_{-3} \times 10^{-5}$	NGC 4472		0.7 ± 0.1	0.8 ± 0.2	$5^{+2}_{-3} \times 10^{-6}$
A478			1.9 ± 0.6	$4^{+4}_{-2} \times 10^{-4}$	NGC 4636		0.19 ± 0.03	0.35 ± 0.07	$6 \pm 2 \times 10^{-5}$
A611			2.4 ± 0.8	$1.4^{+0.5}_{-0.6} \times 10^{-4}$	NGC 4782			1.4 ± 0.4	$1.4^{+0.6}_{-0.9} \times 10^{-5}$
A1795			1.6 ± 0.5	$8^{+12}_{-3} \times 10^{-4}$	NGC 5044		0.27 ± 0.07	0.37 ± 0.07	$9^{+3}_{-5} \times 10^{-5}$
A1835			3 ± 1	$0.004^{+0.005}_{-0.002}$	NGC 5813		0.28 ± 0.04	0.35 ± 0.07	$3.7^{+1.0}_{-0.9} \times 10^{-5}$
A2029			4 ± 1	$2.0^{+1.3}_{-0.7} \times 10^{-4}$	NGC 5846		0.29 ± 0.05	0.45 ± 0.09	$1.6^{+0.6}_{-1.1} \times 10^{-5}$
A2052			1.4 ± 0.4	$9^{+10}_{-2} \times 10^{-4}$	NGC 6269			1.5 ± 0.5	$8^{+3}_{-6} \times 10^{-6}$
A2199		0.7 ± 0.1	1.4 ± 0.4	$0.0015^{+0.0015}_{-0.0005}$	NGC 6338			1.0 ± 0.3	$9^{+3}_{-6} \times 10^{-5}$
A2390			2.6 ± 0.9	0.03 ± 0.03	PKS 0745			2.2 ± 0.7	$0.006^{+0.006}_{-0.002}$
A2597			0.8 ± 0.2	$7^{+9}_{-3} \times 10^{-4}$	PKS 1404			0.6 ± 0.1	$3^{+3}_{-1} \times 10^{-4}$
A2667			1.7 ± 0.6	$1.1 \pm 0.4 \times 10^{-4}$	RXC J0352			0.9 ± 0.2	0.0013 ± 0.0004
A4059			1.9 ± 0.6	$4^{+4}_{-2} \times 10^{-4}$	RXC J1459			3 ± 1	0.003 ± 0.001
Centaurus		0.34 ± 0.06	1.2 ± 0.3	$5^{+4}_{-2} \times 10^{-5}$	RXC J1524			1.3 ± 0.4	$7 \pm 2 \times 10^{-4}$
Cygnus A	2.7 ± 0.7			$0.007^{+0.004}_{-0.002}$	RXC J1558			2.4 ± 0.8	$0.0016^{+0.0007}_{-0.0006}$
HCG62			0.5 ± 0.1	$6^{+9}_{-4} \times 10^{-5}$	Sérsic 159			1.4 ± 0.4	$0.004^{+0.005}_{-0.002}$
Hercules A			1.6 ± 0.5	$0.0016^{+0.0021}_{-0.0007}$	UGC 408			0.35 ± 0.07	$8 \pm 6 \times 10^{-5}$
Hydra A			1.0 ± 0.3	$0.004^{+0.002}_{-0.001}$	Zw 2089			1.1 ± 0.3	0.008 ± 0.002
M84	$0.85^{+0.09}_{-0.08}$			$1.0^{+1.4}_{-0.6} \times 10^{-5}$	Zw 2701			1.4 ± 0.4	0.003 ± 0.001
M87	6.6 ± 0.4			$7^{+5}_{-1} \times 10^{-6}$	Zw 3146			1.6 ± 0.6	$0.03^{+0.04}_{-0.01}$
M89		0.43 ± 0.07	0.27 ± 0.05	$5 \pm 2 \times 10^{-5}$					

arrived at somewhat different conclusions. Allen et al. (2006) found a strong trend between jet power and an estimate of the Bondi accretion rate based on circumnuclear X-ray properties whereas the sample analysed by Rafferty et al. (2006) required greater extrapolation in to the Bondi sphere making their conclusions on Bondi accretion highly uncertain. Nevertheless, using energetic arguments, they found that Bondi power accretion was unable to fuel the most powerful jets unless their black holes were much larger than implied by the M–σ relation. This question is crucial for understanding the relationship between jet power and nuclear emission; therefore, here we re-analyse data for a subsample of 13 systems where we have resolution close to the Bondi sphere. This subsample includes the nine galaxies targeted by Allen et al. (2006) and four additional objects with new, deeper *Chandra* observations (Table 4).

Assuming spherical symmetry and negligible angular momentum, the Bondi rate, $\dot{M}_{\rm B}$, is the accretion rate for a black hole embedded in an atmosphere of temperature, T, and density, n_e, (Bondi 1952) and can be expressed as

$$\frac{\dot{M}_{\rm B}}{{\rm M_\odot\,yr^{-1}}} = 0.012 \left(\frac{k_B T}{\rm keV}\right)^{-3/2} \left(\frac{n_e}{\rm cm^{-3}}\right) \left(\frac{M_{\rm BH}}{10^9\,{\rm M_\odot}}\right)^2 \qquad (2)$$

for an adiabatic index $\gamma = 5/3$. This accretion occurs within the Bondi radius, $r_{\rm B}$, where the gravitational potential of the black hole dominates over the thermal energy of the surrounding gas,

$$\frac{r_{\rm B}}{\rm kpc} = 0.031 \left(\frac{k_B T}{\rm keV}\right)^{-1} \left(\frac{M_{\rm BH}}{10^9\,{\rm M_\odot}}\right). \qquad (3)$$

The Bondi accretion rate is therefore an estimate of the rate of accretion from the hot ICM directly on to the black hole and depends on the temperature and density of the cluster atmosphere at the Bondi radius.

The projected cluster spectra, extracted from a series of annuli as described in Section 2.3, were deprojected using the model-independent spectral deprojection routine DSDEPROJ (Sanders & Fabian 2007; Russell, Sanders & Fabian 2008). Assuming only spherical symmetry, DSDEPROJ starts from the blank-sky background-subtracted spectra and uses a geometric method (Fabian et al. 1981; Kriss, Cioffi & Canizares 1983) to subtract the projected emission off the spectrum from each successive annulus. The resulting deprojected spectra were each fitted in XSPEC with an absorbed single-temperature MEKAL model to determine the temperature and density of the gas, as described in Section 2.3. Several of the selected clusters have clear evidence for multiple temperature components in the inner regions (e.g. M87, Forman et al. 2005; Centaurus, Fabian et al. 2005) and it is likely that deeper exposures of other clusters in the

Table 4. Bondi parameters for the selected subsample of targets.

Target	D_L (Mpc)	$T(r_B)$ (keV)	r_B (kpc)	$n_e(r_B)$ (cm^{-3})	$\dot{M}_B$ ($M_\odot\ yr^{-1}$)	P_B (10^{43} erg s^{-1})	P_{cav} (10^{42} erg s^{-1})
A2199	132.3	1.10 ± 0.07	0.020 ± 0.001	$1.1^{+0.8}_{-0.6}$	$0.006^{+0.004}_{-0.003}$	4 ± 2	9^{+4}_{-2}
Centaurus	49.3	0.41 ± 0.04	0.028 ± 0.002	$0.4^{+0.3}_{-0.2}$	$0.002^{+0.002}_{-0.001}$	0.51 ± 0.06	14^{+7}_{-4}
HCG62	59.3	0.31 ± 0.03	0.058 ± 0.006	$0.3^{+0.3}_{-0.004}$	$0.006^{+0.006}_{-0.000}$	5 ± 2	6^{+4}_{-2}
M84	17.0	0.34 ± 0.01	0.084 ± 0.003	$0.41^{+0.10}_{-0.01}$	$0.020^{+0.005}_{-0.001}$	13 ± 1	$1.1^{+0.9}_{-0.4}$
M87	17.0	0.52 ± 0.04	0.42 ± 0.04	0.23 ± 0.05	0.35 ± 0.07	200 ± 40	8^{+7}_{-3}
M89	17.0	0.35 ± 0.01	0.041 ± 0.002	$0.6^{+0.7}_{-0.5}$	$0.007^{+0.008}_{-0.006}$	5 ± 4	$0.3^{+0.2}_{-0.1}$
NGC 507	71.6	0.49 ± 0.02	0.048 ± 0.002	$0.8^{+1.8}_{-0.5}$	$0.02^{+0.04}_{-0.01}$	20 ± 10	19^{+14}_{-7}
NGC 1316	25.4	0.343 ± 0.007	0.0267 ± 0.0005	$1.3^{+1.6}_{-0.9}$	$0.006^{+0.008}_{-0.004}$	5 ± 4	$0.9^{+0.8}_{-0.4}$
NGC 4472	17.0	0.372 ± 0.007	0.061 ± 0.001	0.5 ± 0.2	$0.014^{+0.006}_{-0.005}$	9 ± 3	$0.7^{+0.5}_{-0.3}$
NGC 4636	17.0	0.23 ± 0.02	0.028 ± 0.002	$0.20^{+0.03}_{-0.05}$	$0.0009^{+0.0001}_{-0.0002}$	0.5 ± 0.1	$0.27^{+0.15}_{-0.09}$
NGC 5044	40.1	0.31 ± 0.01	0.0290 ± 0.0009	$0.3^{+0.5}_{-0.1}$	$0.002^{+0.003}_{-0.001}$	2 ± 1	$1.3^{+0.8}_{-0.4}$
NGC 5813	28.4	0.33 ± 0.01	0.0288 ± 0.0009	$0.28^{+0.18}_{-0.09}$	$0.0016^{+0.0010}_{-0.0005}$	1.0 ± 0.4	$0.7^{+0.6}_{-0.3}$
NGC 5846	24.5	0.378 ± 0.009	0.0256 ± 0.0006	$0.4^{+0.4}_{-0.3}$	$0.002^{+0.002}_{-0.001}$	1.3 ± 1.0	$1.6^{+1.2}_{-0.6}$

subsample will also produce robust detections of multiphase gas. However, given the available range in exposure depth, a uniform method with a single-temperature model was used to determine the emission-weighted average temperature of the ICM in the cluster centre. We also generated deprojected electron density profiles with finer radial binning from the surface brightness profiles and incorporating the temperature and metallicity variations (e.g. Cavagnolo et al. 2009). The finer binned density profiles are consistent with the broader binned results as expected and were used to determine the Bondi accretion rate.

The profiles trace the cluster parameters to radii within an order of magnitude of the Bondi radius and therefore some extrapolation is required. Note that although the Bondi radius in M87 is resolved by *Chandra*, a significant region is affected by pileup and the PSF from the jet knot HST-1 and must be excluded. The temperature profiles were generally found to flatten in the central regions of these systems. We have therefore assumed that the temperature at the accretion radius has only decreased by a further factor of 2 from the innermost temperature bin. Using equation (3), the Bondi radius was calculated from this innermost temperature value and the black hole mass. Dynamical black hole mass estimates were used where available. For comparison with Allen et al. (2006), stellar velocity dispersions from the HyperLeda Database[4] (Paturel et al. 2003) were then used to calculate black hole masses for the rest of the subsample (Tremaine et al. 2002). Only HCG62 did not have a dynamical or velocity mass estimate and the *K*-band magnitude was used (Section 2.5). Tremaine et al. (2002) find an intrinsic dispersion of 0.25–0.3 dex in $\log(M_{BH})$ in the $M_{BH}-\sigma$ relation, which dominates the error in the measurement of the velocity dispersion.

The deprojected electron density continues to increase in the cluster centre and was therefore extrapolated to the Bondi radius using several different model profiles. Three different models were considered: a power-law model continuing a steep density gradient to r_B, a β-model flattening to a constant and a shallowing Sérsic profile with $n = 4$. These models were fitted to the density profile and used to calculate the gas density at r_B. Inner cavity substructure produced some sharp decreases in the deprojected density profile in several clusters. The density models were therefore fitted to all points within the central few kpc to smooth over substructure that is difficult to correctly deproject. No model produced a significantly better fit for each cluster, except for the Centaurus cluster where the β-model is significantly preferred. The density at r_B is therefore given as a range of likely values from the power-law model upper limit to the β-model or Sérsic model lower limit (Table 4). Using equation (2), the Bondi accretion rate was calculated from the density and temperature at r_B and the black hole mass. The density profiles were also integrated from the Bondi radius to 1 arcsec to calculate the predicted flux in this region. This was consistent with the observed flux in this region for each object analysed (Sun 2009a,b).

2.7 Radio point source flux

We also compared the nuclear X-ray flux with the radio core flux for a subset of the sample to try to determine the origin of the nuclear X-ray emission. Radio observations were available for 22 sources in our sample which allowed us to reliably distinguish ongoing core activity. If the sole source of the X-ray flux is in the base of a jet, a direct relationship between the radio and X-ray core flux would be expected.

Nine of the sources in this subsample were observed simultaneously at *C* and *X* bands with the ATCA (project C1958, PI Edge). All but one of the remaining sources were observed at the *C* band with the VLA-C array (various projects, PI Edge), with the last source (A478) having been observed simultaneously at *L* and *X* bands with the VLA-A array (project AE117). For each BCG, the radio-SED was further populated with data from the major radio catalogues (including but not limited to: AT20G at 20 GHz, NVSS/FIRST at 1.4 GHz, SUMSS at 0.843 GHz, WENSS/WISH at 0.325 GHz, VLSS at 0.074 GHz). Additional fluxes were found by searches around the radio-peak coordinates in both the NED and HEASARC online data bases. All literature fluxes were individually scrutinized to ensure reliable matches. Where the synthesized beam size was considered limiting, leading to source confusion, data were discarded. Four of the sources have VLBA observations at *C* band.

Core flux contributions were calculated by considering both the morphology and SEDs of each of the sources. The VLBA *C*-band observations provided direct measurements of the core flux. For the remainder, the SEDs were decomposed into two major components;

[4] http://leda.univ-lyon1.fr/

a flatter spectrum, active component attributed to ongoing activity within the core of the AGN and a steeper spectrum component, most dominant at lower frequencies attributed to either past AGN activity or alternate acceleration mechanisms (e.g. radio lobes, mini-haloes, etc.).

Where a clearly resolved core was present in the observations, two-component SEDs were fitted directly. For sources which were resolution limited at *C* band, spectral breakdown of the SEDs was performed on a case-by-case basis. Consideration was given to extent seen at other wavelengths, spectral shape and variability, with the proviso that variable sources are more likely to contain a strong currently active core. Simple mathematical models were fitted to the SEDs using IDL routines where a strong case could be made for believing distinct components were present. For sources where past and current activity could not be reliably distinguished, limits were placed on the core contribution. Full details of the SED analysis will be presented in Hogan et al. (in preparation).

3 RESULTS

In total, 27 out of 54 BCGs in this sample were found to have X-ray central point sources detected above 3σ in the 3−7 keV energy band. Although this is not a complete sample of objects, central X-ray point sources appear to be common in BCGs with detected X-ray cavities. Fig. 3 shows the distribution of the ratio of X-ray nuclear luminosity in the 2−10 keV energy range to cavity power, L_X/P_{cav}, for the cluster sample. The detected point sources in this sample cover a broad range in radiative efficiency from $L_X/P_{cav} > 0.1$ (e.g. 3C 295) to $L_X/P_{cav} < 10^{-3}$ (e.g. A2199). This distribution presumably reflects a broad range in average accretion rate with the majority accreting in a radiatively inefficient mode i.e. they are ADAFs (see Section 1).

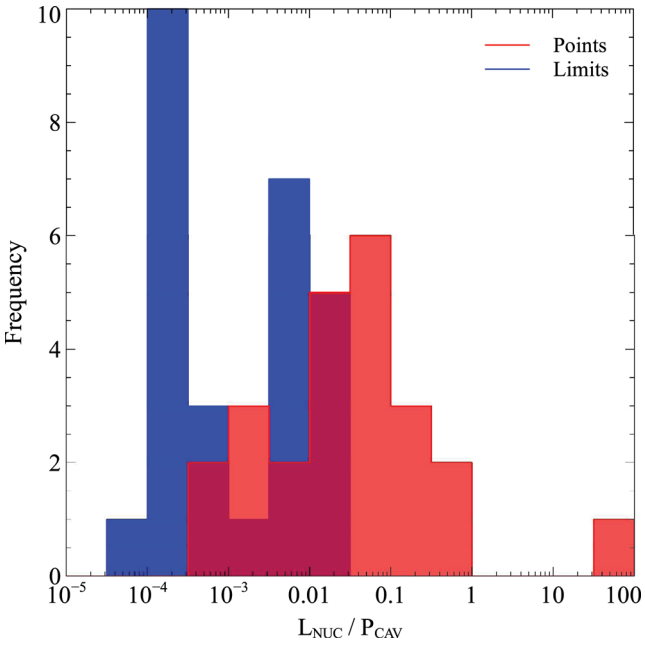

Figure 3. Histogram showing the distribution of the ratio of X-ray point source luminosity to cavity power for the low-luminosity AGN in the sample. Three point sources have no detected cavities and are therefore not included.

3.1 Radiative and cavity power output

Fig. 4 (left) shows a correlation between the nuclear point source 2–10 keV luminosity and the cavity power injected into the surrounding ICM. This correlation was first found by Merloni & Heinz (2007) for a sample of 15 AGN with measured cavity powers, 13 of which also had X-ray point source detections. The scatter in this correlation covers three orders of magnitude therefore the generalized Kendall's τ rank correlation coefficient for censored data (Brown, Hollander & Korwar 1974) from the survival analysis package ASURV Rev 1.3 (Isobe, Feigelson & Nelson 1986; Isobe & Feigelson 1990; Lavalley, Isobe & Feigelson 1992) was used to evaluate its significance. We find a probability of accepting the null hypothesis that there is no correlation between the point source luminosity and the cavity power of $P_{null} = 4 \times 10^{-4}$. Given the substantial difference in the time-scales, i.e. six orders of magnitude, it is surprising to observe a trend at all between these properties and suggests that AGN feedback is persistent.

It is not clear if the systems with upper limits on the point source luminosity form part of this trend, and are only just too faint to detect, or are currently 'off'. We have therefore considered these two scenarios separately using the BCES estimators (Akritas & Bershady 1996) for a linear regression fit to the data points only and the ASURV non-parametric Buckley–James linear regression fit to both the points and upper limits (Buckley & James 1979). Note that this analysis excluded the point sources with no detected cavities in the surrounding ICM as no effective upper limits for the cavity power could be estimated (see Section 2.4). The inclusion of the upper limits produces a shift in the correlation but only a small change in the observed slope, which is consistent within the error. The BCES orthogonal best fit was found to be $\log(P_{cav}) = (0.69 \pm 0.08)\log(L_X) + 15 \pm 3$ compared to the ASURV Buckley–James best fit of $\log(P_{cav}) = (0.7 \pm 0.1)\log(L_X) + 14$. The majority of the sample analysed are in a radiatively inefficient accretion mode where the mechanical cavity power dominates the radiative output from the AGN. The observed slope shows that the radiative efficiency of the X-ray nucleus increases with increasing cavity power.

For comparison, we have included three quasars from the literature that are located in luminous cool core clusters to illustrate this increase in radiative efficiency. H1821+643 (Russell et al. 2010), IRAS 09104+4109 (Cavagnolo et al. submitted) and 3C 186 (Siemiginowska et al. 2005, 2010) each have a total radiative power of $L \sim 10^{47}$ erg s^{-1} that exceeds their cavity power by at least an order of magnitude. Fig. 4 (left) shows that these sources appear to form an extension of the trend to much higher cavity powers and presumably much higher accretion rates. This implies that as the accretion rate rises black holes become more radiatively efficient.

Following Merloni & Heinz (2007), we also estimate the bolometric point source luminosity for all sources in the sample and scale the luminosity and cavity power by the Eddington luminosity (Fig. 4 right). The SED for low-luminosity AGN lacks the 'big blue bump' of emission dominating higher accretion rate sources and is likely to be dominated by the emission at hard X-ray energies. Vasudevan & Fabian (2007) find a typical bolometric correction for low-luminosity sources of the order of ∼10; however, for ease of comparison we adopt the same factor of 5 as Merloni & Heinz (2007). Fig. 4 (right) shows the correlation between the bolometric point source luminosity and the cavity power where both quantities are scaled by the Eddington luminosity (Section 2.5). The non-parametric Buckley–James linear regression method from ASURV software was used to determine the best-fitting relation for both the

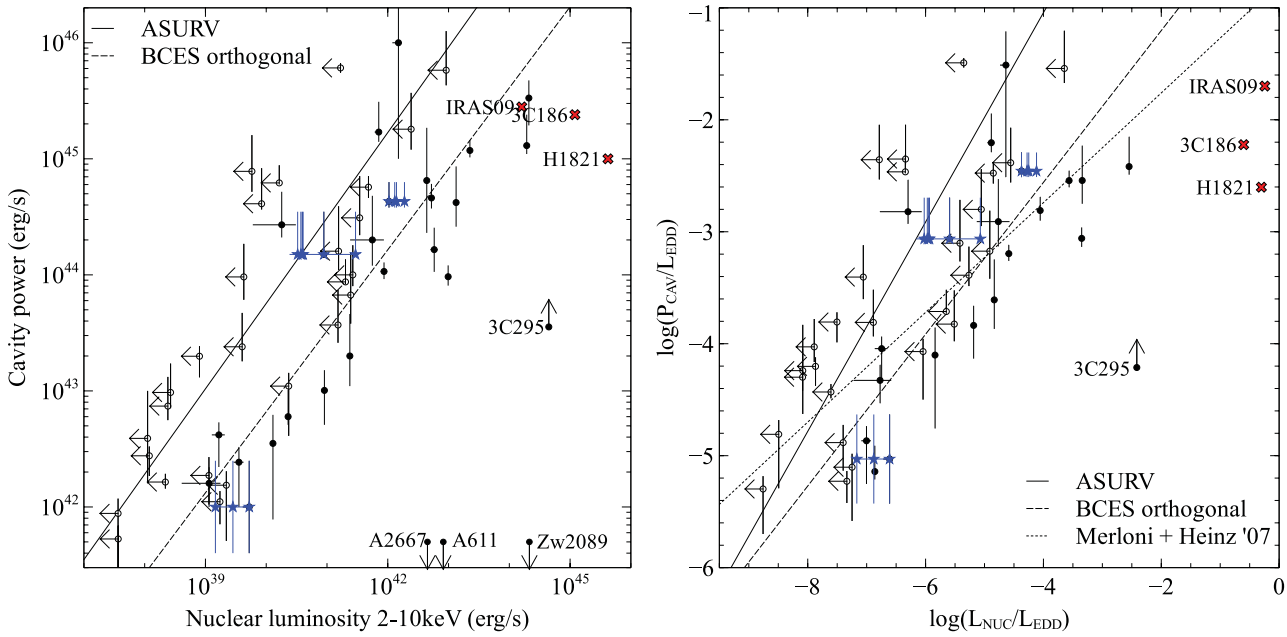

Figure 4. Left: nuclear X-ray luminosity in the energy range 2−10 keV calculated using the spectroscopic method versus cavity power from the literature. Right: bolometric nuclear luminosity versus cavity power where both quantities are scaled by the Eddington luminosity. Clusters with confirmed point source detections are shown by the filled circles and upper limits are shown by the open circles. Three quasar sources from the literature are included for comparison (red crosses). The variable sources are shown as blue stars (see Section 3.5). The best fit to both points and upper limits using the ASURV Buckley & James (1979) estimator for censored data is shown by the solid line. The BCES orthogonal fit to the data points only is shown by the dashed line. The best fit from Merloni & Heinz (2007) is shown as a dotted line and is consistent with the BCES fit to the data points within the errors.

points and the upper limits (Buckley & James 1979). The best-fitting slope of $\log(L_{\rm cav}/L_{\rm Edd}) \propto 0.9 \log(L_{\rm nuc}/L_{\rm Edd})$ is significantly steeper than that found by Merloni & Heinz (2007) (Fig. 4 right). Using the BCES estimators linear regression fit to only the data points we determine that the best fit is consistent with the Merloni & Heinz (2007) result within the errors. The inclusion of a large number of upper limits results in a significant difference in the slope of the correlation. We show in Section 3.5 that three systems vary by up to an order of magnitude over a 10 year timespan. This is apparently a significantly contributing factor to the scatter to which the Merloni & Heinz (2007) sample was not sensitive. Another factor that may be contributing is beaming of the central X-ray source, which is discussed in detail in Merloni & Heinz (2007).

3.2 Selection effects

It is also clear that the scatter in this correlation between the nuclear X-ray luminosity and the cavity power is underestimated by our sample selection. Sources were selected primarily on the detection of cavities in X-ray observations and therefore sources with point sources but no cavities are generally missed from the lower right of Fig. 4. Three such sources, Zw 2089, A611 and A2667, were added to the sample to illustrate this selection bias. Note that the upper limits on the cavity powers are only illustrative, not quantitative (Section 2.4). Whilst the observation of A2667 is shallow at only 8 ks, both A611 and Zw 2089 have sufficiently deep X-ray observations that would detect signs of any cavities or feedback-related substructure in the cluster cores. In particular, Zw 2089 contains a bright X-ray point source and appears very relaxed with smooth extended X-ray emission and no likely cavity structures. However, if cavities in this system are emerging along our line of sight, they will be particularly difficult to detect. There could be a significant number of similar systems with bright point sources but no cavity structures, which will tend to increase the scatter in the observed correlation further.

The brightness and temperature of the surrounding cluster emission could also introduce another selection effect to this analysis. Point sources are identified by a significant detection of emission in a hard X-ray band, 3–7 keV, above the background cluster (Section 2.3). Bright, high-temperature clusters will have more emission in this energy band than fainter, cooler systems therefore potentially making it more difficult to detect a point source above this background. Fig. 5 shows that for systems with strong background cluster emission in the 3–7 keV band there are several sources (labelled) with higher upper limits. This suggests that an AGN in these BCGs would have to be brighter to be detected than in BCGs with fainter emission in this energy band. However, only a handful of sources in our sample appear to be affected so this will only slightly reduce the scatter in Fig. 4.

The selection bias in our sample will have a significant impact on the best-fitting linear relation determined for the correlation in Fig. 4 (right). This is illustrated by the difference in slope between the Buckley–James linear regression in this analysis and the result found by Merloni & Heinz (2007). We have therefore not drawn any further conclusions from the slope of this correlation but considered the possible sources of the scatter, which covers at least three orders of magnitude.

3.3 Uncertainty in cavity power and black hole masses

The measured cavity powers available in the literature for a particular system are often found to differ by factors of a few up to an order of magnitude. This can be due to new observations of an object, which reveal more cavities or better constrain the shapes of previously known cavities. It also reflects the inherent systematic uncertainty and judgement of the extent of the cavity volume (see

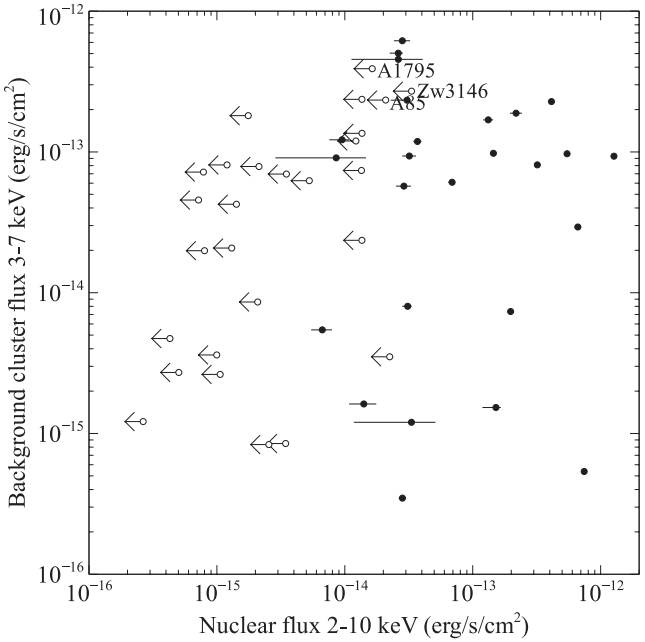

Figure 5. Nuclear X-ray flux in the 2–10 keV energy band versus the cluster flux from a surrounding annulus in the 3–7 keV energy band.

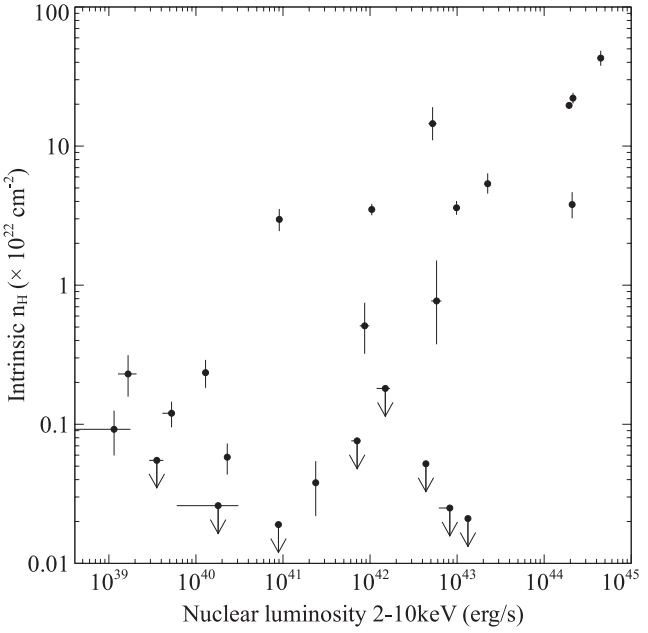

Figure 6. Nuclear X-ray luminosity versus the intrinsic absorption of the point source for a subset of objects with sufficient counts for a reasonable spectral fit.

e.g. McNamara & Nulsen 2012). Cavities with bright rims, such as those in the Hydra A (e.g. McNamara et al. 2000) and A2052 (e.g. Blanton et al. 2011), have a well-defined shape, although some uncertainty still exists over the line-of-sight extent and whether the inner, outer or middle of the rims should be used. Most cavities do not have complete rims and their extent is difficult to constrain given the rapid decline in X-ray surface brightness with radius (Bîrzan et al. 2012). The cavity power for A2390 has a particularly large error, $P_{\rm cav} = 1.0^{+1.0}_{-0.9} \times 10^{46}$ erg s^{-1}, because the extent of cavities is difficult to determine from the X-ray image. As discussed in Section 2.4, the cavity power for 3C 295 is likely to have been significantly underestimated and this is therefore an outlier. For the majority of the sources, uncertainty in the cavity power is unlikely to introduce scatter greater than an order of magnitude. Also, although the black hole masses are likely to be a significant source of additional error for Fig. 4 (right), the scatter in Fig. 4 (left) is comparably large and does not depend on black hole mass.

3.4 Absorption

Another significant source of uncertainty in the X-ray point source fluxes may be attributable to photoelectric absorption by intervening gas within the galaxy or in a circumnuclear torus. This would cause a systematic underestimate of the point source luminosity. The amount of intrinsic absorption can be determined from spectral fitting but only for the brighter sources in our sample. Fig. 6 shows the intrinsic absorbing column density as a function of nuclear X-ray luminosity for 25 of the 27 detected low-luminosity AGN. There were insufficient counts for the detections of 3C 388 and A2667 to constrain the intrinsic absorption. The intrinsic $n_{\rm H}$ values cover a range from relatively unobscured sources with $n_{\rm H} < 10^{21}$ cm^{-2}, such as M87, up to heavily obscured narrow-line radio galaxies with $n_{\rm H} > 10^{23}$ cm^{-2}, such as 3C 295. It is therefore plausible that a number of the non-detected sources could be moderately or heavily absorbed. This would account for some of the scatter in Fig. 4 and potentially render these sources undetectable in the 0.5–7 keV energy band accessible to *Chandra*.

Fig. 6 has interesting astrophysical implications as well. The most luminous sources in our sample often contain large columns of cold intervening gas along the line of sight, in some cases exceeding 10^{23} atoms cm^{-2}. It is unknown where along the line of sight this gas lies but it is likely to be close to the nucleus. This implies the existence of a supply of cold gas to fuel the nucleus. The range of intrinsic absorption may be related in part to the geometry of cold gas relative to the central point source. For example the point sources in Hydra A and NGC 4261 are peering through circumnuclear gas discs that are highly inclined to the plane of the sky (e.g. Jaffe & McNamara 1994; Dwarakanath, Owen & van Gorkom 1995). Furthermore, the path towards the core in Cygnus A is strongly reddened by intervening dust and presumably accompanying gas located within 800 pc of the nucleus (Vestergaard & Barthel 1993).

Using a subset of example upper limits at different redshifts, we determined that if these undetected sources had an intrinsic absorption of 10^{22}–10^{23} cm^{-2}, their true luminosity could be factors of up to a few greater than the observed upper limit. Intrinsic absorption of $\sim 10^{24}$ cm^{-2} and above is required for the true luminosity of the source to be an order of magnitude or more greater than the observed upper limit. For a significant amount of the scatter in Fig. 4 to be generated by intrinsic absorption, a large fraction of the upper limits must therefore be Compton thick. These sources would then represent a very different population to the detected point sources in this sample.

Although a large fraction of the upper limits in this sample could be significantly absorbed (e.g. Maiolino et al. 1998; Fabian & Iwasawa 1999; Risaliti, Maiolino & Salvati 1999; Brandt & Hasinger 2005; Guainazzi, Matt & Perola 2005), this still seems unlikely to completely account for the three to four orders of magnitude scatter in Fig. 4. Reliably identifying Compton-thick AGN and determining their intrinsic luminosity is difficult (e.g. Comastri 2004; Nandra & Iwasawa 2007; Alexander et al. 2008). Gandhi et al. (2009) (see also Hardcastle, Evans & Croston 2009) found a linear relation between

the 2−10 keV X-ray luminosity of the AGN and the 12 μm mid-IR luminosity. Somewhat surprisingly, Gandhi et al. (2009) also found that the eight Compton-thick sources in their sample did not deviate significantly from this trend. We might therefore expect that a large fraction of the undetected sources in our sample have high IR luminosities as the absorbed power from the nucleus is re-radiated at these energies.

However, for BCGs at the centre of cool core clusters, a significant fraction of the observed IR luminosity is likely due to star formation (e.g. Egami et al. 2006; O'Dea et al. 2008; Quillen et al. 2008). Egami et al. (2006) found that the BCGs in A1835, A2390 and Zw 3146, all with point source upper limits in our sample, are IR bright and have SEDs typical of star-forming galaxies. Quillen et al. (2008) identify several BCGs as having very strong AGN contributions in the IR, such as Zw 2089, but in more modest cases this is difficult to disentangle from star formation. Interestingly, Quillen et al. (2008) find that the BCG in Sérsic 159-03 is IR faint with only an upper limit on the IR star formation rate. Therefore, despite being one of the strongest upper limits in our sample (Fig. 4), Sérsic 159-03 does not appear to host a heavily absorbed AGN. Without detailed SEDs to disentangle the AGN contribution from star formation in these objects it is difficult to systematically determine if a significant fraction of the point source upper limits are heavily absorbed sources. However, even if this is the case, it is unlikely to explain the three orders of magnitude scatter in Fig. 4 (see also Evans et al. 2006).

3.5 X-ray variability

Another source of scatter is variability in the nuclear X-ray luminosity. The cavity power is averaged over the cavity ages, which are estimated from the sound crossing time or the buoyant rise time and are typically 10^7–10^8 yr (Bîrzan et al. 2004). However, the nuclear power is expected to be variable on time-scales much shorter than this. In contrast to the majority of Seyferts, low-luminosity AGN usually do not exhibit strong, rapid variability on time-scales of less than a day. However, variability of order a factor of a few on time-scales of months to years is likely (e.g. Ptak et al. 1998; Pian et al. 2010; Young et al. 2012). The effect of variability on the trends in Fig. 4 is very much like that of relativistic beaming (Merloni & Heinz 2007). A subset of the clusters in our sample have multiple observations spaced by several years in the *Chandra* archive, which we searched for possible variations in the X-ray point source flux.

The point source flux was calculated for each observation using both the photometric and spectroscopic methods described in Section 2.3. For the spectroscopic method, the differing depth of the observations could produce variations in the cluster parameters determined from surrounding annuli, which would add scatter to the measured point source fluxes. However, by fixing the cluster parameters in each observation to those determined from the deepest exposure available, we verified that this did not significantly alter the results. The point source fluxes for this subsample are shown in Table 5. The best-fitting intrinsic absorption and photon index are shown for each exposure but the fluxes were calculated using the values of these parameters from the deepest exposure of that source. No significant change in the intrinsic absorption or the photon index was found for the sources analysed.

Fig. 7 shows that the point source flux was found to significantly vary in A2052, Hydra A and M84. The flux in A2052 was observed to decline by an order of magnitude over the 10 years traced by the *Chandra* archive. Hydra A shows a more modest decline by a factor of ∼2 over 5 years, whereas for M84 a decline by a factor of ∼3.5 drop in flux occurs in only 6 months. Note that for Hydra A the earliest ACIS-I observation in 2000 was not included (obs. ID 575) as this data set was taken during the soft proton damage to the detector. Furthermore, three of the non-variable systems in Table 5 could be

Table 5. Point source fluxes and key parameters for each source tested for variability. The photometric point source flux, F_P, and the spectroscopic point source flux, F_S, are both given in the 2−10 keV energy band. A spectroscopic flux measurement could not be produced for M84 obs. ID 401 because the 1 ks exposure was too short.

Target	Obs. ID	Date	Aimpoint	Exposure (ks)	$n_{H,z}$ (10^{22} cm^{-2})	Γ	F_P (10^{-14} erg cm^{-2} s^{-1})	F_S (10^{-14} erg cm^{-2} s^{-1})
A2052	890	03-09-2000	S3	30.5	<0.014	$2.06^{+0.08}_{-0.06}$	12.6 ± 0.4	10 ± 1
	5807	24-03-2006	S3	123.8	<0.019	$2.00^{+0.09}_{-0.07}$	3.8 ± 0.1	$3.1^{+0.2}_{-0.3}$
	10 879	05-04-2009	S3	80.0	0	1.9	2.2 ± 0.1	1.1 ± 0.3
	10 478	25-05-2009	S3	119.0	$0.03^{+0.05}_{-0.03}$	2.2 ± 0.2	2.1 ± 0.1	1.4 ± 0.3
	10 477	05-06-2009	S3	59.0	0	1.9	2.4 ± 0.1	$1.4^{+0.3}_{-0.4}$
	10 479	09-06-2009	S3	63.9	0	1.9	2.2 ± 0.1	$1.3^{+0.3}_{-0.3}$
A2390	500	08-10-2000	S3	8.8	0	1.9	0.9 ± 0.4	<1.1
	4193	11-09-2003	S3	70.6	$0.1^{+0.2}_{-0.1}$	1.9	1.4 ± 0.1	$0.9^{+0.1}_{-0.2}$
Hydra A	576	02-11-1999	S3	17.4	$4.3^{+0.8}_{-0.6}$	1.9	36 ± 3	26 ± 2
	4969	13-01-2004	S3	62.1	$3.0^{+0.8}_{-0.7}$	$1.7^{+0.4}_{-0.3}$	27 ± 1	18 ± 1
	4970	22-10-2004	S3	94.6	$2.2^{+0.6}_{-0.5}$	1.2 ± 0.3	24 ± 1	$14.5^{+0.8}_{-0.7}$
M84	401	20-04-2000	S3	1.7	0	1.9	7 ± 1	–
	803	19-05-2000	S3	25.5	0.17 ± 0.04	2.1 ± 0.1	8.6 ± 0.4	$8.2^{+0.4}_{-1.2}$
	5908	01-05-2005	S3	45.1	$0.12^{+0.03}_{-0.02}$	2.13 ± 0.09	17.5 ± 0.4	15^{+1}_{-3}
	6131	07-11-2005	S3	35.8	$0.17^{+0.08}_{-0.07}$	2.2 ± 0.3	4.9 ± 0.3	$4.2^{+0.3}_{-0.4}$
NGC 5044	798	19-03-2000	S3	14.3	0	1.9	2.4 ± 0.4	<0.2
	9399	07-03-2008	S3	82.5	$0.23^{+0.08}_{-0.07}$	1.9	2.6 ± 0.2	$1.4^{+0.4}_{-0.3}$
PKS 0745	2427	16-06-2001	S3	17.9	0	1.9	3.0 ± 0.6	$2.0^{+0.6}_{-1.8}$
	12 881	27-01-2011	S3	116.0	<0.08	1.8 ± 0.2	4.8 ± 0.3	$2.6^{+0.2}_{-0.4}$
PKS 1404	1650	07-06-2001	S3	7.1	0.07 ± 0.05	2.4 ± 0.2	24 ± 1	22 ± 2
	12 884	03-01-2011	S3	83.5	0.04 ± 0.02	2.01 ± 0.06	21.4 ± 0.4	19.8 ± 0.7

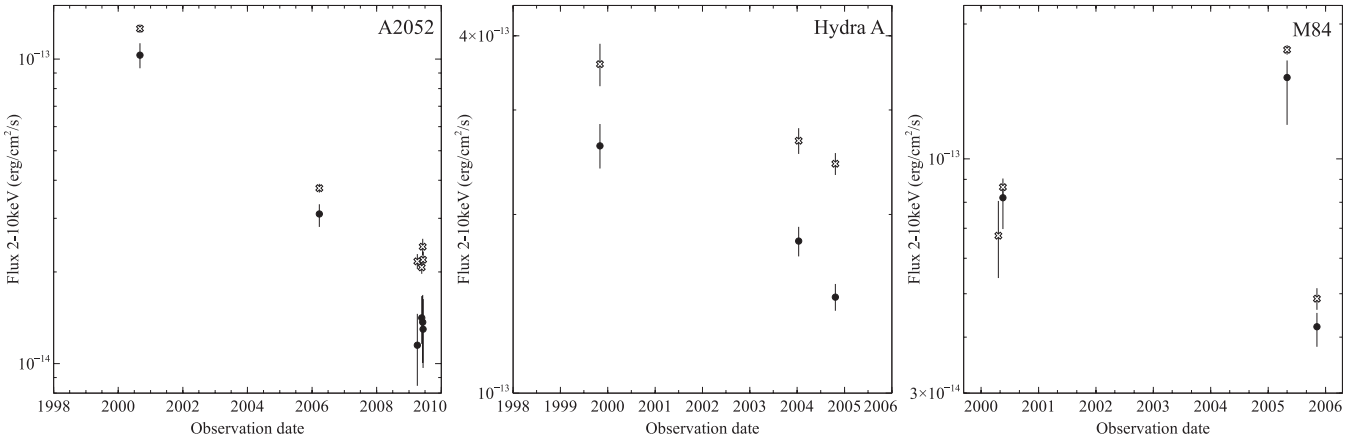

Figure 7. AGN flux variability in A2052 (left), Hydra A (centre) and M84 (right). The point source fluxes are calculated using both the photometric (open crosses) and spectroscopic methods (filled circles). Note that a spectroscopic flux measurement could not be produced for M84 obs. ID 401 because the 1 ks exposure was too short.

variable by factors of 1.5–3 over a decade but the existing data are only sufficient to place limits. This analysis is generally limited by the availability of suitably spaced observations of sufficient depth in the *Chandra* archive but suggests that a significant fraction of AGN in BCGs may be varying on time-scales of months to a few years. The bright central point sources in the Perseus cluster and M87 have long been known to be variable at X-ray wavelengths (e.g. Rothschild et al. 1981; Harris, Biretta & Junor 1997). Another source in our sample, NGC 4261, has been found to be variable on short 3–5 ks time-scales in a study by Sambruna et al. (2003). This variability is likely to be a significant source of scatter in the correlation between nuclear X-ray luminosity and cavity power. The cavity power is an average of the AGN activity over 10^7–10^8 yr whereas the point source luminosity is likely to fluctuate significantly on much shorter time-scales potentially by orders of magnitude.

The shape of the nuclear spectrum from Hydra A is dramatically different from those of A2052 and M84. Hydra A's spectrum falls sharply below 2 keV while the flux below 2 keV in A2052 and M84 continues to rise. This strong decline in flux shortwards of 2 keV in Hydra A is due to a large column of intervening gas that may be associated with the large circumnuclear disc (e.g. Dwarakanath et al. 1995; Hamer et al., in preparation). We also searched for a change in the shape of the nuclear spectrum as the sources varied. Fig. 8 shows the spectrum for each observation of each point source found to have significantly varying X-ray flux. The cluster background was subtracted from each spectrum using a surrounding annulus. The spectra are remarkably consistent between the observations and suggest that despite the large variations in flux, particularly in A2052, there has been no significant change in the shape of the spectrum.

3.6 Nuclear radio luminosity

Fig. 9 (left) shows no apparent correlation between the nuclear X-ray flux and the 5 GHz radio core flux. There does appear to be an approximately linear trend between the nuclear X-ray luminosity and the radio luminosity (Fig. 9, right), although the X-ray flux is on average an order of magnitude larger. However, it is highly likely that this trend is due to redshift selection effects given the lack of a correlation in the flux–flux plot.

Whilst care was taken to provide reliable core contributions to the overall radio flux density at *C* band, there are of course limitations. A variety of facilities were used to obtain the flux measurements used in the SEDs. Whilst this variety was considered in the decompositions, there will undoubtedly be situations where the true core contribution is lower than found in this analysis. This is due

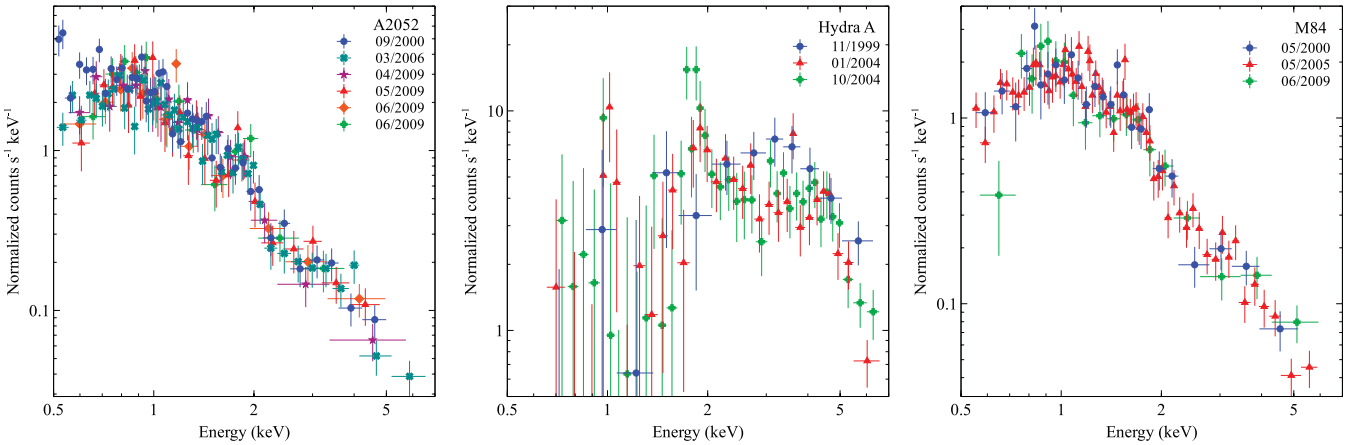

Figure 8. Point source spectra normalized to the flux at 2 keV for A2052 (left), Hydra A (centre) and M84 (right). Note that a spectrum could not be produced for M84 obs. ID 401 because the 1 ks exposure was too short.

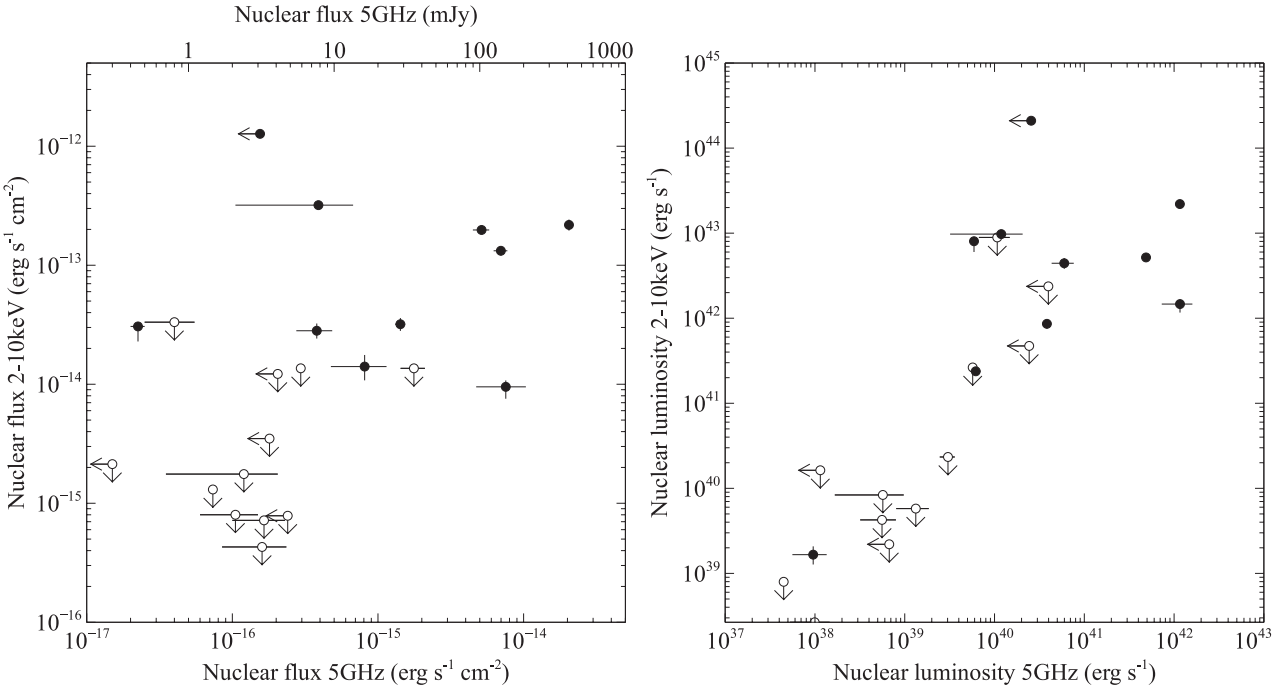

Figure 9. X-ray 2–10 keV versus radio 5 GHz flux (left) or luminosity (right). Nuclear X-ray detections are shown by the solid points and X-ray upper limits are shown by the open points.

to contamination from extended emission in the lower resolution observations which is not adequately accounted for in the models. Similarly, for the highly core-dominated sources, large observed variability may lead to the radio core flux being underestimated at the epoch of the X-ray observations. These shortcomings will be a contributing factor to the scatter seen in Fig. 9. It should be noted however that the radio core contributions used here are taken from a larger sample of radio-loud BCGs analysed by Hogan et al (in preparation). Of this larger sample, 26 are observed with the VLBA and strong agreement is seen between the direct VLBA core measurements and the SED-breakdown-derived core contributions. Finally, many of the radio cores are self-absorbed so the 5 GHz flux may significantly underestimate the total radio power of the core. There is also likely to be significant scatter due to variability in both the X-ray and the radio flux. With no clear trend between the X-ray and radio nuclear flux it appears less likely that the X-ray emission originates from the base of a jet, although emission from the ADAF is possible (Mościbrodzka et al. 2009).

3.7 Bondi accretion

The deprojected temperature and electron density profiles for the Bondi subsample of 13 systems are shown in Fig. 10. For each cluster we have marked the location of the Bondi radius and shown that the radial profiles are within roughly an order of magnitude of this. For the clusters that overlap with the Allen et al. (2006) sample, we generally find good agreement between the density and temperature profiles. The Centaurus cluster profiles were found to differ significantly because Allen et al. (2006) used a 35° wide sector to the north-east of the nucleus compared to our full annuli, which included the complex structure west of the nucleus. The temperature profile for NGC 5846 is also significantly different in shape but we note that the central values used for the Bondi analysis are consistent. We used a more recent, deep observation of this source and the results are consistent with the Machacek et al. (2011) analysis. The Bondi radius, accretion rate and cavity powers calculated from the temperature and density profiles for each of the selected systems are shown in Table 4. Following Allen et al. (2006), we calculated the cavity power for only the inner two cavities of each object that are currently being inflated by the central AGN.

Fig. 11 (left) shows the Bondi power plotted against the cavity power generated by the inner two cavities in each system. This shows a significant weakening of the trend found by Allen et al. (2006) driven mainly by a difference in the estimates of cavity volume. For most of these sources, our cavity powers are consistent with Allen et al. (2006) within the large errors of a factor of 2−3 on these values. However, for M84, M89, NGC 4472 and NGC 507, our cavity powers are lower than those of Allen et al. (2006) by factors of up to an order of magnitude (see also Merloni & Heinz 2007). This was partly due to the availability of new, deeper observations of M84, NGC 507 and NGC 4472, which more clearly revealed the cavity extent. Allen et al. (2006) also used 1.4 GHz radio images to determine the edges of the cavities and this may have caused significant differences from our primarily X-ray method. Our new estimates of X-ray cavity power agree with estimates from Cavagnolo et al. (2010), Rafferty et al. (2006) and O'Sullivan et al. (2011b). It is not clear whether cavity powers will be more accurate when calculated using the X-ray or the radio observations; therefore, we have also included Fig. 11 (right) showing our analysis of the Bondi accretion power versus the cavity powers from Allen et al. (2006). This plot shows a larger scatter than Allen et al. (2006) found and this scatter is due solely to differences in how we and Allen et al. (2006) calculated the central density. The vertical 'error bars' represent the range of Bondi powers from the three best-fitting models and the mid-point is marked as no model provides a significantly better fit. The exception is the Centaurus cluster where the β-model is significantly preferred and we therefore used the Bondi power from the best-fitting β-model with its associated errors.

The Kendall's τ rank correlation was used to determine if these two measures of cavity power are significantly correlated with the

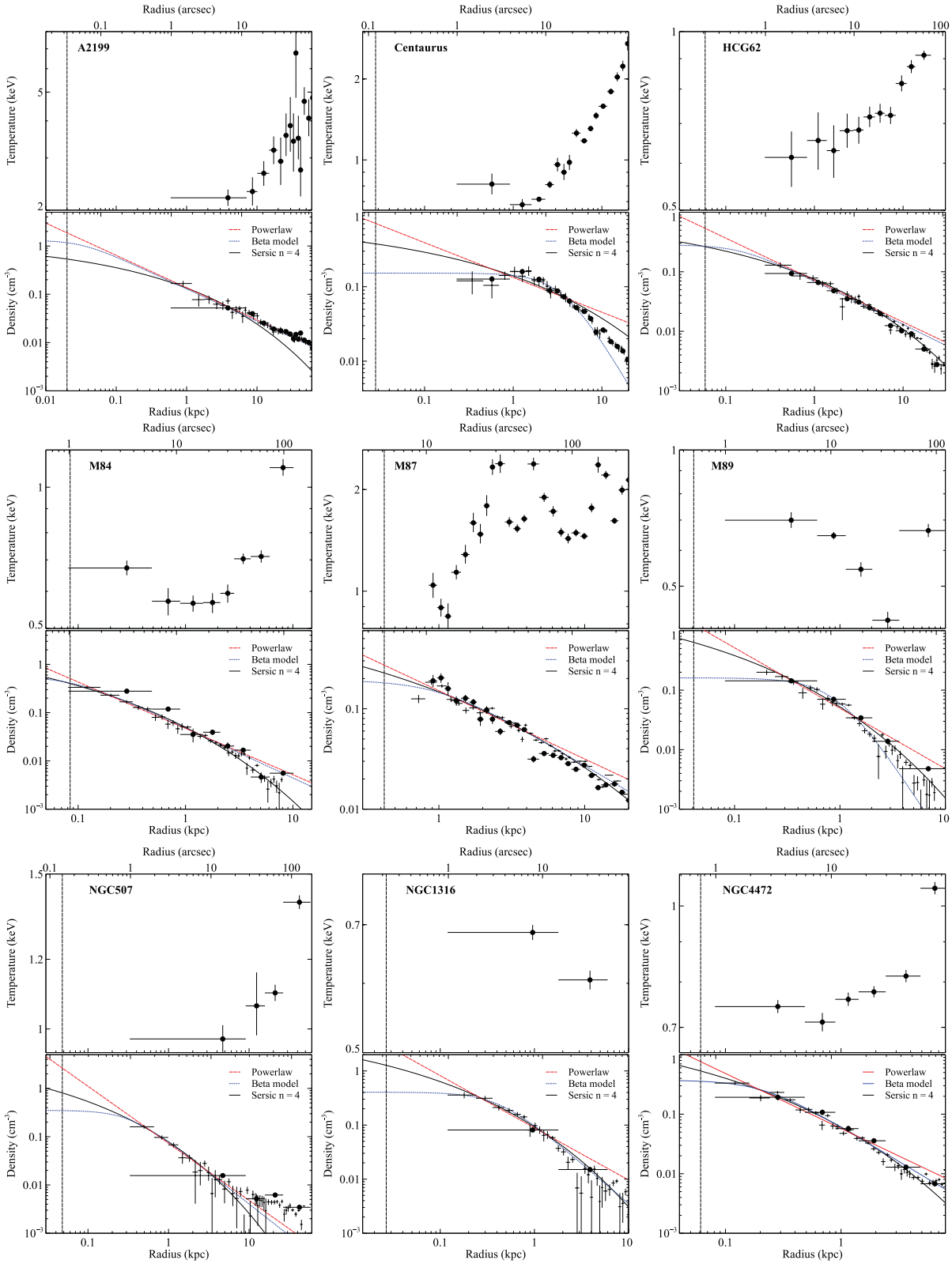

Figure 10. Deprojected temperature and electron density profiles of a subset of the cluster sample for which the cluster properties can be resolved at radii within an order of magnitude of the Bondi radius (shown by the vertical dashed line).

Bondi accretion rate. For our estimates of cavity power, we find no significant correlation with $\tau = 0.2$. For the estimates of cavity power from Allen et al. (2006), we calculate $\tau = 0.7$ and reject the null hypothesis of no correlation at 95 per cent confidence but not at 99 per cent confidence. This analysis therefore suggests weaker evidence for a trend between the cavity power and Bondi accretion power, primarily due to the uncertainty in estimates of the cavity volumes.

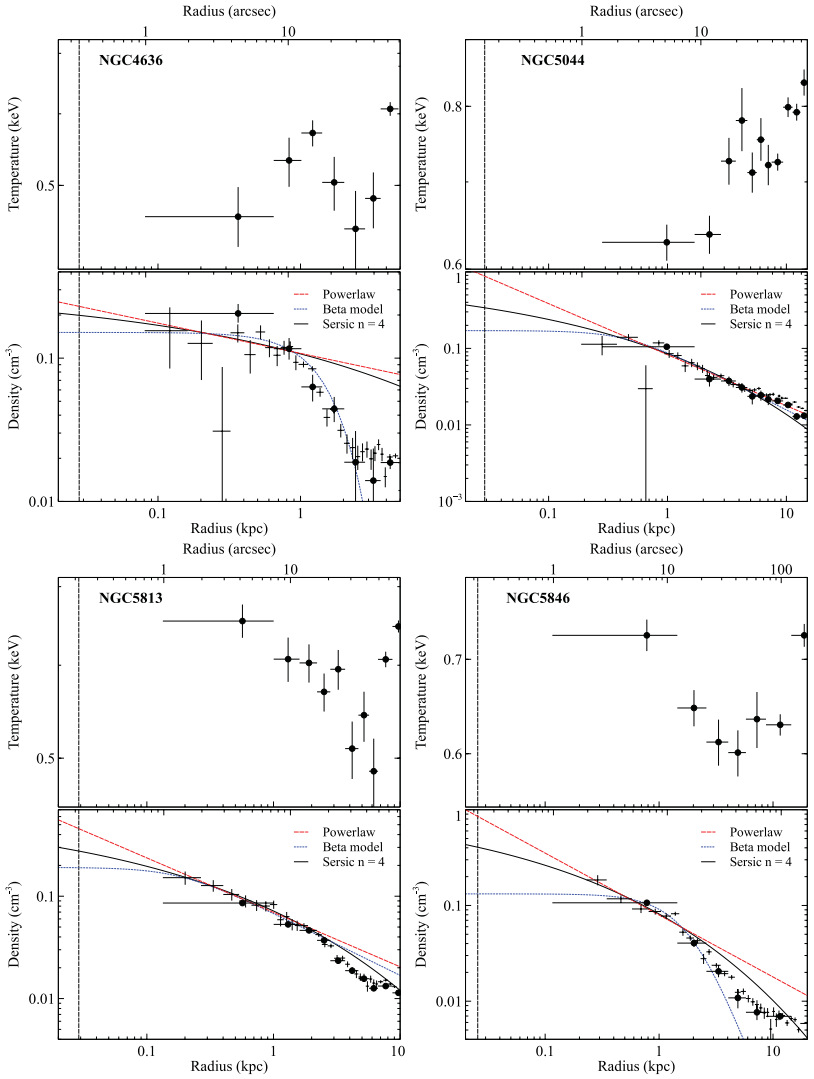

Figure 10 – *continued*

4 DISCUSSION

X-ray central point sources appear to be common in BCGs hosting X-ray cavities. We find a detection fraction of ∼50 per cent for the BCGs in our sample. The majority of these sources are radiatively inefficient with required average accretion rates of only 10^{-5}–$10^{-2}\dot{M}_{\rm Edd}$. The nuclear X-ray luminosity for these sources was observed to correlate with the AGN cavity power, which is surprising given the vastly different time-scales for these quantities. Cavity power is averaged over the bubble ages, typically 10^{7}–10^{8} yr, while the nuclear X-ray luminosity is an instantaneous measurement and we have shown that this can vary significantly on shorter time-scales of months to years. The scatter in this correlation covers over three orders of magnitude. A significant fraction of this scatter is likely due to X-ray variability but absorption and uncertainty in the cavity power estimates will also contribute.

The interpretation of these results is complicated by the uncertainty in the origin of the nuclear X-ray emission. The X-ray emission may originate from the accretion disc corona, from the base of a parsec-scale jet or a combination of the two although another origin is also possible. However, the nuclear X-ray emission is generally considered a probe of accretion power, whether it is from the accretion flow or from the jet (e.g. Falcke & Biermann 1995; Heinz & Sunyaev 2003). Therefore, the observed $L_{\rm X}-P_{\rm cav}$ correlation suggests the accretion power roughly scales with the cavity power over long time-scales with the large scatter reflecting variability on shorter time-scales.

4.1 Duty cycle of activity

It is also not clear if systems with only upper limits on the point source luminosity are simply faint or currently 'off'. As shown in Fig. 4, whether the upper limits form the faint end of the detected source population or are instead a different population of 'off' systems can have a significant impact on the correlation's slope and scatter. Approximately ∼50 per cent of the sample do not have detected nuclear X-ray emission. It is likely that at least some sources are simply a little too faint to be detected, particularly if they are embedded in bright cluster emission (see Section 3.2). These objects may therefore still be consistent with the observed $P_{\rm cav}-L_{\rm X}$ correlation. However, objects such as MS0735 and Sérsic 159 have upper limits on their radiative luminosities a factor of 1000 below that expected from this trend and are effectively 'off'.

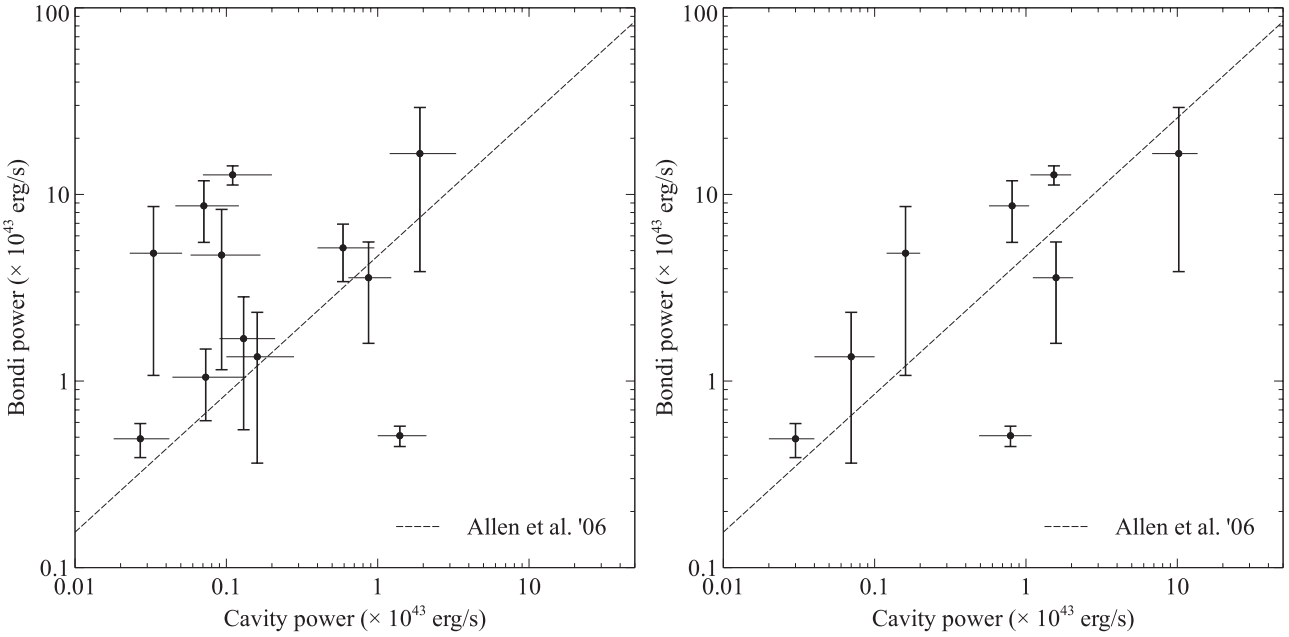

Figure 11. Bondi accretion power versus cavity power. Left: cavity power from this analysis. Right: cavity power from Allen et al. (2006). The best-fitting relation from Allen et al. (2006) is shown as a dashed line. The errors on the Bondi accretion power represent the range of Bondi powers from the three best-fitting models and the mid-point is marked as no model provides a significantly better fit over the others. The exception is the Centaurus cluster where the best-fitting β-model result was used.

Hlavacek-Larrondo & Fabian (2011) considered a sample of highly radiatively inefficient nuclei in clusters with powerful AGN outbursts, including MS0735, and suggested several explanations including absorption and variability. We have found significant variability for several sources in a subset of our sample, which could indicate a cycle of activity, but do not find absorption to be as important. Although we caution that this sample is by no means complete, the fraction of detections to non-detections indicates a duty cycle of at least ∼50 per cent in systems with recent AGN outbursts. If we consider only the 31 sources that overlap with the Rafferty et al. (2006) sample, we find a similar detection fraction of at least 40 per cent. This suggests that roughly half of all systems undergoing an AGN outburst in the last $\sim 10^8$ yr have evidence of ongoing accretion. Mendygral, Jones & Dolag (2012) found that simulations with a jet duty cycle of 50 per cent, cycling on and off with a 26 Myr period, produced multiple cavity pairs with a similar morphology to observations (see also O'Neill & Jones 2010; Mendygral, O'Neill & Jones 2011). For complete samples of clusters, the fraction with detected X-ray cavities implies a duty cycle of at least ∼60−70 per cent (Dunn & Fabian 2006; Bîrzan et al. 2009, 2012).

4.2 Radiative efficiency and evidence for a transition luminosity

Although it is not clear if the upper limits form the faint end of the detected source population or are a separate population of 'off' systems, the best-fitting models for these two possibilities have a consistent slope in Fig. 4 (left). This slope shows an increase in radiative efficiency with the mean accretion rate. The quasars included for comparison form an extension of this trend from cavity power-dominated to radiation-dominated sources. Studies have also shown that the radio loudness of low-luminosity AGN to luminous quasars is inversely correlated with the mass accretion rate (e.g. Ho 2002; Terashima & Wilson 2003; Panessa et al. 2007; Sikora, Stawarz & Lasota 2007). SMBHs appear to become more efficient at releasing energy through jets as their accretion rate drops. Hlavacek-Larrondo et al. (2013) also find strong evolution in the nuclear X-ray luminosities of SMBHS hosted by BCGs such that the fraction of BCGs with radiatively-efficient nuclei is decreasing over time.

Observational evidence suggests that the accretion process is largely similar for both stellar mass and SMBHs and therefore we could potentially use studies of X-ray binaries to understand accretion in AGN (e.g. Maccarone et al. 2003; Merloni et al. 2003; Falcke et al. 2004). X-ray binaries are broadly classified into low-hard and high-soft states, which relate to the accretion disc properties and variation in the accretion rate can trigger state transitions (e.g. Remillard & McClintock 2006). In the low-hard state, the accretion rate is low, the accretion disc is optically thin and radiatively inefficient. The mechanical power of the radio jet dominates the radiative power and the X-ray and radio fluxes are correlated (e.g. Gallo, Fender & Pooley 2003; Fender & Belloni 2004). Observations of X-ray binaries have shown that as the accretion rate rises above ~ 0.01–$0.1 \dot{M}_{\rm Edd}$ the source makes a spectral transition from the low-hard to the high-soft state (e.g. Nowak 1995; Done, Gierliński & Kubota 2007). In this state the X-ray emission is dominated by an optically thick, geometrically thin accretion disc and the radio emission drops dramatically suggesting the outflow is suppressed (e.g. Fender et al. 1999).

Fig. 12 shows the radiative and cavity power output as a function of the required mean accretion rate for our AGN sample, where all quantities are scaled by the Eddington rate. The mean accretion rate was calculated from the cavity power plus the bolometric luminosity of the point source and scaled by the Eddington accretion rate,

$$\frac{\dot{M}}{\dot{M}_{\rm Edd}} = \frac{(P_{\rm cav} + L_{\rm bol})}{L_{\rm Edd}}. \quad (4)$$

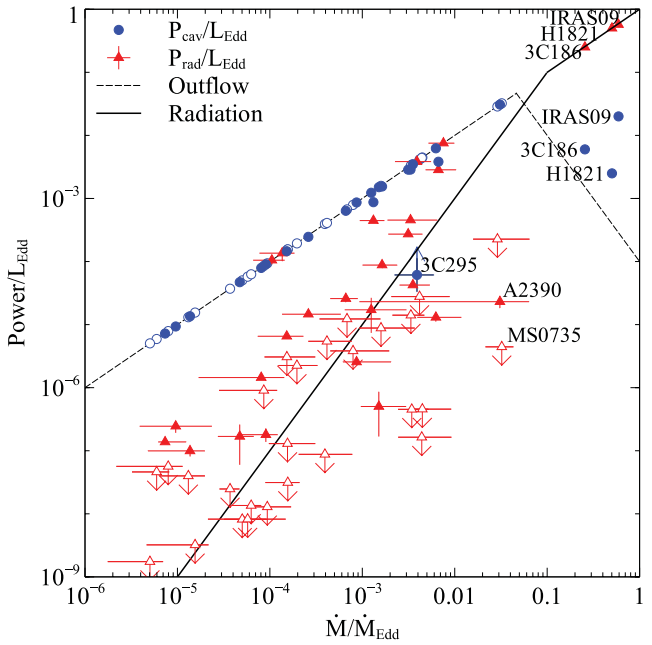

Figure 12. The required mean accretion rate scaled by the Eddington rate, $\dot{M}/\dot{M}_{Edd}$, plotted against the cavity power (blue circles) and the radiative power (red triangles) scaled by the Eddington luminosity. Therefore, there are two points for each source. Detected nuclear X-ray point sources are shown by the solid symbols and upper limits are shown by the open symbols. Quasar sources are labelled. The radiation and outflow model lines are illustrative only and show a transition from outflow domination at low accretion rates to radiative domination at high accretion rates (from Churazov et al. 2005, Fig. 1).

L_{bol} was calculated as shown in Section 3.1 for the low-luminosity AGN and was taken from the literature for the quasars. Note that for most of the sources considered, L_{bol} is insignificant compared to P_{cav} and the required mean accretion rate is dictated by the cavity power. The quasars are the obvious exceptions. Values for each source are given in Table 3. There are two points for each source on the plot showing both the cavity power and the radiative power. For sources where the radiative power or the cavity power dominates the output, the corresponding points will, by definition, lie on a line of equality. This produces a clear line of points along Power$/L_{Edd} = \dot{M}/\dot{M}_{Edd}$ in Fig. 12.

The illustrative model from Churazov et al. (2005) of a change from a radiatively inefficient, outflow-dominated mode to a radiation-dominated mode has been shown for comparison in Fig. 12. Fig. 12 shows a trend of increasing radiative efficiency with mean accretion rate (see also Fig. 4). The radiative and mechanical power outputs converge and become comparable at an Eddington rate of a few per cent. For accretion rates below $\sim 0.1\dot{M}_{Edd}$, the cavity power dominates the radiative output, which is a factor of 10−1000 times lower. Above $\sim 0.1\dot{M}_{Edd}$, a transition apparently occurs where mechanical power drops suddenly and the radiative power strongly dominates. This strong transition is seen in three objects: H1821+643, IRAS 09104+4109 and 3C 186. These are quasars in the centres of galaxy clusters, few are known but they show this intriguing and potentially very important effect where they transition from mechanically dominated to radiation-dominated AGN. This is precisely the behaviour expected when the accretion rate increases and an object transitions from an ADAF to a geometrically thin and optically thick disc. The AGN in our sample therefore appear to show the same qualitative behaviour with variation in accretion rate found for stellar mass black holes.

However, there is significant scatter in the trend for radiatively inefficient sources, some of which may be due to variability in the X-ray flux. There are also outliers on the plot, notably MS0735 and A2390. A2390 may have overestimated cavity power and thus could move to the left. MS0735 was noted as anomalous to Churazov's scenario in Churazov et al. (2005). In this case the issue could be related to powering by the spin of the black hole (McNamara et al. 2009) where the spin energy is tapped more efficiently than mc^2 (e.g. Cao 2011; McNamara, Rohanizadegan & Nulsen 2011; Tchekhovskoy, Narayan & McKinney 2011; McKinney, Tchekhovskoy & Blandford 2012). This would imply greater jet power per accreted mass than objects powered directly by accretion, moving it to the left in Fig. 12. It is also possible that the unknown value of ϵ, the conversion efficiency between mass and energy $P = \epsilon \dot{M} c^2$, is a large source of scatter, particularly as it is applied to mechanical power. We have assumed in equation (4) that ϵ is tied between the radiation and cavity power and divides out but this is of course not necessarily true. Nevertheless, the increasing nuclear brightness relative to mechanical power is solid. And the transition to quasars does depend on power output and by inference, $\dot{M}$. This picture is also a simplification of stellar mass black hole state transitions. Observed transitions from the low-hard to the high-soft state in X-ray binaries are accompanied by an intense and rapid radio outburst, which has no obvious analogy in our AGN model (e.g. Fender, Belloni & Gallo 2004, but see also Czerny et al. 2009).

4.3 Accretion power

The source of fuel for the observed AGN activity has been the subject of considerable debate. There is, in general, sufficient cold gas in BCGs to fuel the range of observed jet powers (Edge 2001; Salomé & Combes 2003; Soker 2008; Donahue et al. 2011). However, Bondi accretion directly from the cluster's hot atmosphere is appealing because it can provide both a steady fuel supply and a simple feedback mechanism. Although whilst the gas density is high enough to supply sufficient fuel to low-power jet systems through Bondi accretion (e.g. Allen et al. 2006), this is difficult to achieve for high-power jets ($>10^{45}$ erg s^{-1}; Rafferty et al. 2006; Hardcastle, Evans & Croston 2007; McNamara et al. 2011). Using a sample of nearby systems, Allen et al. (2006) found a correlation between the cavity power and Bondi accretion rate suggesting that a few per cent of the rest-mass energy of material crossing the Bondi radius emerges in the jets.

In our analysis of 13 systems, including the Allen et al. (2006) sample, we found a significantly larger scatter in the correlation between the cavity power and Bondi accretion rate. This was primarily due to differences in our calculation of the density at the Bondi radius and estimates of the cavity power. Calculation of the density at the Bondi radius required an extrapolation of this profile over an order of magnitude in radius for each object in our sample. We used three different model density profiles for the extrapolation and found each provided a similarly good fit, with the exception of the Centaurus cluster where a β-model was significantly better. This fit was extended to cover a few kpc rather than just the central points as cavity substructure close to the centre affected the deprojection of the density profile. The use of three equally plausible extrapolations of the density profile produced different estimates of the density at the Bondi radius and increased the scatter in the Bondi accretion rate compared to Allen et al. (2006). Deeper

observations of several clusters, showing the cavity extent more clearly, significantly altered the cavity power measured for those objects. We have therefore found weaker evidence for a trend between the cavity power and Bondi accretion rate.

Bondi accretion is energetically a plausible mechanism for fuelling the lower powered radio sources in our sample. However, it is insufficient to fuel the most powerful systems (Hardcastle et al. 2007; McNamara et al. 2011). There are also theoretical issues with Bondi accretion that include the ability to shed angular momentum and the zero central pressure requirement (Proga & Begelman 2003; Pizzolato & Soker 2005, 2010; Soker 2008; Narayan & Fabian 2011). For a more complete discussion see McNamara & Nulsen (2012).

In view of the high column densities found for many objects in this sample, which are consistent with significant levels of cold circumnuclear gas, and the prevalence of cold molecular gas in cD galaxies (e.g. Edge 2001; Salomé & Combes 2003), we suggest that cold gas fuelling is a likely source of accretion power in these objects. Nevertheless, we cannot rule out or exclude Bondi accretion, which could play a significant role, particularly in low-power jets (Allen et al. 2006).

4.4 Nuclear X-ray emission mechanism

The origin of the observed nuclear X-ray emission is not currently understood. Observed correlations between the X-ray and radio core luminosities provide the strongest support for a non-thermal jet-related origin (e.g. Fabbiano, Gioia & Trinchieri 1989; Canosa et al. 1999; Hardcastle & Worrall 1999). Radio and optical luminosity correlations for FR I nuclei also support this conclusion (Chiaberge, Capetti & Celotti 1999) and multiwavelength SEDs for these sources can be modelled by synchrotron and synchrotron self-Compton emission from a jet (e.g. Capetti et al. 2002; Yuan et al. 2002; Chiaberge et al. 2003b). However, Donato, Sambruna & Gliozzi (2004) show that a significant fraction of sources with strong optical jet emission do not have an X-ray component potentially indicating different physical origins. The detection of broad Fe Kα lines and rapid variability on ks time-scales favours an accretion flow origin (e.g. Gliozzi, Sambruna & Brandt 2003). Radio and X-ray correlations do not necessarily imply a common origin for the emission as accretion processes and jets are likely to be correlated phenomena (e.g. Begelman, Blandford & Rees 1984). Merloni et al. (2003) and Falcke et al. (2004) argued that these correlations are part of a 'Fundamental Plane' linking radio and X-ray emission to black hole mass but differ on whether this reveals trends in accretion or jet physics (e.g. Körding, Falcke & Corbel 2006; Hardcastle et al. 2009; Plotkin et al. 2012).

4.4.1 Jet origin

Wu, Yuan & Cao (2007) analysed the SEDs of eight FR I sources including two of the variable sources in our sample, A2052 (3C 317) and M84 (3C 272.1). They found that the emission in M84 is dominated by a jet and the ADAF model predicts too hard a spectrum at X-ray energies. A2052 appears to have a comparable contribution from the jet and the ADAF. These two sources have very different accretion rates: for A2052 $\dot{M}/\dot{M}_{\rm Edd} = 9^{+10}_{-2} \times 10^{-4}$ and for M84 $\dot{M}/\dot{M}_{\rm Edd} = 5^{+8}_{-4} \times 10^{-6}$. Yet they both experience significant variations in nuclear flux on time-scales of months to years.

Strong flux variability on time-scales of 1–2 months is seen from both the core and the jet knot HST-1 in M87 (e.g. Harris et al. 1997; Harris et al. 2006). From 2000 to 2009, HST-1 is the site of a massive X-ray, UV and radio flare. During this period, the X-ray emission from HST-1 dominates the nucleus and rises and falls by an order of magnitude (Harris et al. 2009). The nuclear variability is characterized by Harris et al. 2009 as 'flickering' with changes in flux of the order of a factor of a few over time-scales of months to years. It is not clear if the nuclear X-ray emission is due to the inner unresolved jet or the accretion flow. The magnitude and time-scales of the X-ray flux variability found in A2052, Hydra A and M84 are therefore consistent with that observed in M87. Interestingly, *HST* UV observations of the nucleus in A2052 find the luminosity increased by a factor of 10 from 1994 to 1999 (Chiaberge et al. 2002). This period was then followed by a decrease in the X-ray luminosity by a similar factor from 2000 to 2010, which could indicate a flaring event similar to that experienced by HST-1.

Sambruna et al. (2003) found variability with *XMM–Newton* on 3–5 ks time-scales in the FR I radio galaxy NGC 4261, which is also part of our sample. For an ADAF, the X-ray emission is radiated from a relatively large volume and variation is expected on time-scales longer than around a day (Ptak et al. 1998; Terashima et al. 2002). The observed variability time-scale in NGC 4261 is around two orders of magnitude shorter than the ADAF light crossing time suggesting that the variable component is more likely to be associated with the inner jet. Unfortunately, the count rate in the *Chandra* observations of our sample is generally not large enough to search the light curve of each individual observation for flux variation. We also do not find any significant variation in the spectral properties of the three variable sources identified in our subsample.

4.4.2 ADAF origin

ADAF models predict trends between the nuclear radio and X-ray luminosities that scale as $L_{\rm R} \propto L_{\rm X}^{0.6}$ and $\dot{M} \propto L_{\rm X}^{0.5}$ (Yi & Boughn 1998). Assuming $\dot{M} \propto P_{\rm cav}$, this scaling is consistent with the slope shown in Fig. 4. Although the slope between $L_{\rm R}$ and $L_{\rm X}$ shown in Fig. 9 appears to be steeper than $L_{\rm R} \propto L_{\rm X}^{0.6}$, the lack of a flux–flux correlation and the large uncertainties suggest that this trend is unreliable (see Section 3.6). It is therefore worthwhile to consider the consequences of emission from an ADAF.

Fig. 13 compares the X-ray point source luminosities with predictions from ADAF models at different accretion rates (Merloni et al. 2003). The nuclear X-ray luminosity scales very close to linearly with black hole mass allowing us to scale up these models to the required $\sim 10^9\,{\rm M}_\odot$. For low accretion rates, the $2-10\,{\rm keV}$ emission includes inverse Compton scattering of soft synchrotron or disc photons and a bremsstrahlung component at higher energies. At higher accretion rates, the Compton-scattered component dominates as the optical depth rises and cooling processes become more efficient. The exact scaling of $L_{2-10\,{\rm keV}}$ with $\dot{M}/\dot{M}_{\rm Edd}$ will depend on the parameters chosen for the model, such as the viscosity, magnetic pressure and electron heating fraction. Therefore, Merloni et al. (2003) obtain a single power-law fit $L_{2-10\,{\rm keV}} \propto (\dot{M}/\dot{M}_{\rm Edd})^{2.3}$ from their ADAF models for comparison with observational data.

The required mean accretion rate was calculated from the cavity power plus the radiative power as shown in equation (4). For most of the sources considered, $L_{\rm bol}$ is insignificant compared to $P_{\rm cav}$ and the required mean accretion rate is dictated by the cavity power. The three quasars are the exceptions to this. The majority of the observed sources are consistent with the emission expected from an ADAF for black hole masses from 5×10^8 to $5 \times 10^9\,{\rm M}_\odot$. Four sources in our sample have more accurate dynamical black hole masses and

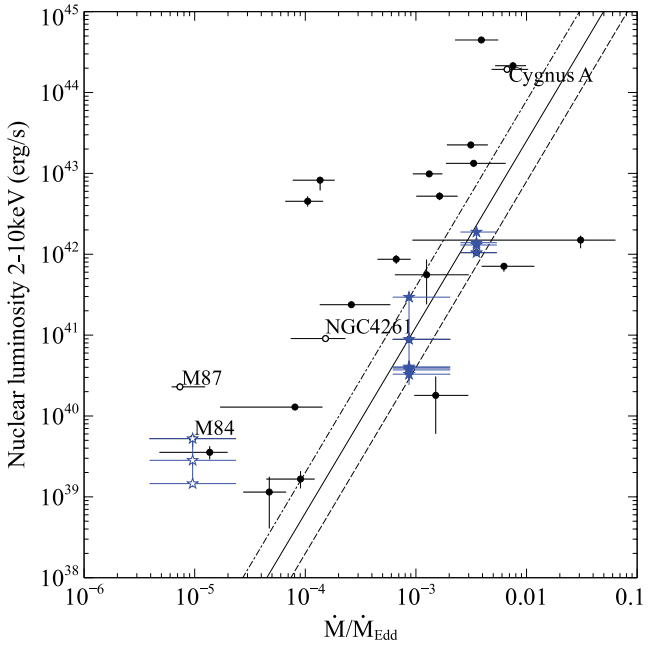

Figure 13. Point source X-ray luminosity versus the inferred accretion rate scaled by the Eddington rate. The lines represent ADAF model predictions from Merloni et al. (2003) for black hole masses of 5×10^8 $M_\odot$ (dashed), 1×10^9 $M_\odot$ (solid) and 5×10^9 $M_\odot$ (dash–dotted). The variable point sources are shown by the blue stars. Sources with dynamical black hole masses are shown by the open symbols (Cygnus A, M84, M87 and NGC 4261).

therefore provide a more reliable constraint when compared with ADAF model predictions. Cygnus A and NGC 4261 have mass accretion rates a factor of 3−5 smaller than the ADAF model predictions for their respective black hole masses. The difference is even greater for M84 and M87 with over an order of magnitude and close to two orders of magnitude discrepancy, respectively. There are several possible reasons for this. The cavity power in M84 is particularly difficult to estimate as the outburst appears to have blown out most of the X-ray atmosphere. The cavity volume and surrounding pressure may therefore have been underestimated. The total mechanical power in M87 has been significantly underestimated as the shock produces an additional 2.4×10^{43} erg s^{-1}, which is four times greater than the cavity power. This would cause M84 and M87 to move to the right in Fig. 13 and closer to the ADAF models. So this translates to a similar increase in the mean accretion rate. The nuclear X-ray emission from M84 and M87 is therefore likely to be consistent with an ADAF given the large uncertainties in the ADAF models. As previously discussed in Section 2.4, the cavity power is likely to have been underestimated for the majority of the systems in this sample and this will tend to move points to the right in Fig. 13.

We therefore conclude that it is plausible that the X-ray point source emission is due to an ADAF but we cannot distinguish between this and a jet origin with the available data. Given the lack of a clear trend between the nuclear radio and X-ray flux it is likely that further progress on this problem will require modelling of the AGN SED (e.g. Wu et al. 2007).

5 CONCLUSIONS

Using archival *Chandra* observations of 57 BCGs, we have investigated the relationship between nuclear X-ray emission and AGN radio jet (cavity) power. Although this is not a complete sample of objects, we find that nuclear X-ray emission is common with roughly half of the sample hosting a detectable X-ray point source. Assuming nuclear X-ray emission indicates active accretion, our study implies that the AGN in systems with recent outbursts are 'on' at least 50 per cent of the time. Furthermore, we examine the correlation between the nuclear X-ray luminosity and the average accretion rate determined from the energy required to inflate the X-ray cavities. This correlation is consistent with the hypothesis that the nuclear X-ray emission traces active accretion in these systems. The majority of the sources in this sample are radiatively inefficient with required mean accretion rates of only 10^{-5}–10^{-2} $\dot{M}_{Edd}$. The nuclear X-ray sources become more luminous compared to the cavity power as the average accretion rate increases. The nuclear X-ray emission exceeds the cavity power when the average accretion rate rises above a few per cent of the Eddington rate, where the AGN power output appears to transition from cavity power dominated to radiation dominated in the three BCGs hosting quasars.

A small subset of the clusters in our sample had multiple archival *Chandra* observations of sufficient depth to search for variability in the nuclear X-ray flux. We found that A2052, M84 and Hydra A were significantly varying by factors of 2–10 on time-scales of 6 months to 10 years. Despite the large variations in flux, we did not find significant change in the shape of the nuclear spectra. This analysis is generally limited by the availability of suitably spaced observations of sufficient depth in the Chandra archive but suggests that a significant fraction of AGN in BCGs may be varying on time-scales of months to a few years. This variability is likely to be a significant source of the large scatter in the observed correlation between the nuclear luminosity and cavity power. Our results suggest that the accretion power roughly scales with the cavity power over long time-scales with the large scatter reflecting the variability on shorter time-scales.

The interpretation of these results is complicated by the uncertainty of the nuclear X-ray emission origin. This emission may originate from the accretion disc corona, from the base of a jet or a combination of both, although other mechanisms are also possible. We discuss the similarity in magnitude and time-scale of the X-ray variability found in A2052, M84 and Hydra A to that observed from both the core and jet knot HST-1 in M87. We also show that the X-ray nuclear luminosity and required mean accretion rate of the systems analysed are consistent with the predictions from ADAF models. We conclude that an ADAF is a plausible origin of the X-ray point source emission but we cannot distinguish between this and a jet origin with the available data.

We have also considered the longstanding problem of whether jets are powered by the accretion of cold circumnuclear gas or accretion from the hot keV atmosphere. For a subsample of 13 nearby systems, the Bondi accretion rate was calculated using three equally plausible model extrapolations of the cluster density profile to the Bondi radius. The results suggest weaker evidence for a trend between the cavity power and the Bondi accretion rate, primarily due to the uncertainty in the cavity volumes. Cold gas fuelling may therefore be a more likely source of accretion power given the high column densities found for many objects in our sample, which are consistent with significant quantities of cold circumnuclear gas, and the prevalence of cold molecular gas in BCGs. However, we cannot rule out Bondi accretion, which may play a significant role, particularly in low-power jets.

ACKNOWLEDGEMENTS

HRR and BRM acknowledge generous financial support from the Canadian Space Agency Space Science Enhancement Program. RAM and ANV acknowledge support from the Natural Sciences and Engineering Research Council of Canada. We thank Paul Nulsen, Avery Broderick, Roderick Johnstone and James Taylor for helpful discussions. We also thank the reviewer for helpful and constructive comments. This work makes use of data products from the Two Micron All Sky Survey, which is a joint project of the University of Massachusetts and the Infrared Processing and Analysis Center/California Institute of Technology, funded by the National Aeronautics and Space Administration and the National Science Foundation. This research has made use of the NASA/IPAC Extragalactic Database (NED) which is operated by the Jet Propulsion Laboratory, California Institute of Technology, under contract with the National Aeronautics and Space Administration.

REFERENCES

Abramowicz M. A., Chen X., Kato S., Lasota J.-P., Regev O., 1995, ApJ, 438, L37
Akritas M. G., Bershady M. A., 1996, ApJ, 470, 706
Alexander D. M. et al., 2008, ApJ, 687, 835
Allen S. W., Ettori S., Fabian A. C., 2001, MNRAS, 324, 877
Allen S. W., Dunn R. J. H., Fabian A. C., Taylor G. B., Reynolds C. S., 2006, MNRAS, 372, 21
Anders E., Grevesse N., 1989, Geochim. Cosmochim. Acta, 53, 197
Arnaud K. A., 1996, in Jacoby G. H., Barnes J., eds, ASP Conf. Ser. Vol. 101, Astronomical Data Analysis Software and Systems V. Astron. Soc. Pac., San Francisco, p. 17
Balmaverde B., Capetti A., Grandi P., 2006, A&A, 451, 35
Balucinska-Church M., McCammon D., 1992, ApJ, 400, 699
Batcheldor D., Marconi A., Merritt D., Axon D. J., 2007, ApJ, 663, L85
Begelman M. C., Blandford R. D., Rees M. J., 1984, Rev. Mod. Phys., 56, 255
Belsole E., Worrall D. M., Hardcastle M. J., Croston J. H., 2007, MNRAS, 381, 1109
Bîrzan L., Rafferty D. A., McNamara B. R., Wise M. W., Nulsen P. E. J., 2004, ApJ, 607, 800
Bîrzan L., Rafferty D. A., McNamara B. R., Nulsen P. E. J., Wise M. W., 2009, in Heinz S., Wilcots E., eds, AIP Conf. Ser. Vol. 1201, The Monster's Fiery Breath: Feedback in Galaxies, Groups and Clusters. Am. Inst. Phys., New York, p. 301
Bîrzan L., Rafferty D. A., Nulsen P. E. J., McNamara B. R., Röttgering H. J. A., Wise M. W., Mittal R., 2012, MNRAS, 427, 3469
Blandford R. D., Begelman M. C., 1999, MNRAS, 303, L1
Blandford R. D., Begelman M. C., 2004, MNRAS, 349, 68
Blanton E. L., Sarazin C. L., McNamara B. R., 2003, ApJ, 585, 227
Blanton E. L., Randall S. W., Clarke T. E., Sarazin C. L., McNamara B. R., Douglass E. M., McDonald M., 2011, ApJ, 737, 99
Bondi H., 1952, MNRAS, 112, 195
Bower R. G., Benson A. J., Malbon R., Helly J. C., Frenk C. S., Baugh C. M., Cole S., Lacey C. G., 2006, MNRAS, 370, 645
Brandt W. N., Hasinger G., 2005, ARA&A, 43, 827
Brown B. W. M., Hollander M., Korwar R. M., 1974, in Proschan F., Serfling R. J., eds, Reliability and Biometry. Society for Industrial and Applied Mathematics, Philadelphia, p. 327
Buckley J., James I., 1979, Biometrika, 66, 429
Canosa C. M., Worrall D. M., Hardcastle M. J., Birkinshaw M., 1999, MNRAS, 310, 30
Cao X., 2011, ApJ, 737, 94
Capetti A., Trussoni E., Celotti A., Feretti L., Chiaberge M., 2002, New Astron. Rev., 46, 335
Cash W., 1979, ApJ, 228, 939
Cavagnolo K. W., Donahue M., Voit G. M., Sun M., 2009, ApJS, 182, 12
Cavagnolo K. W., McNamara B. R., Nulsen P. E. J., Carilli C. L., Jones C., Bîrzan L., 2010, ApJ, 720, 1066
Cavagnolo K. W., McNamara B. R., Wise M. W., Nulsen P. E. J., Brüggen M., Gitti M., Rafferty D. A., 2011, ApJ, 732, 71
Chiaberge M., Capetti A., Celotti A., 1999, A&A, 349, 77
Chiaberge M., Macchetto F. D., Sparks W. B., Capetti A., Allen M. G., Martel A. R., 2002, ApJ, 571, 247
Chiaberge M., Gilli R., Macchetto F. D., Sparks W. B., Capetti A., 2003a, ApJ, 582, 645
Chiaberge M., Gilli R., Capetti A., Macchetto F. D., 2003b, ApJ, 597, 166
Chiaberge M., Capetti A., Macchetto F. D., 2005, ApJ, 625, 716
Churazov E., Forman W., Jones C., Böhringer H., 2000, A&A, 356, 788
Churazov E., Sunyaev R., Forman W., Böhringer H., 2002, MNRAS, 332, 729
Churazov E., Sazonov S., Sunyaev R., Forman W., Jones C., Böhringer H., 2005, MNRAS, 363, L91
Comastri A., 2004, in Barger A. J., ed., Astrophysics and Space Science Library, Vol. 308, Supermassive Black Holes in the Distant Universe. Kluwer, Dordrecht, p. 245
Crawford C. S., Lehmann I., Fabian A. C., Bremer M. N., Hasinger G., 1999, MNRAS, 308, 1159
Croton D. J. et al., 2006, MNRAS, 365, 11
Czerny B., Siemiginowska A., Janiuk A., Nikiel-Wroczyński B., Stawarz Ł., 2009, ApJ, 698, 840
Dalla Bontà E., Ferrarese L., Corsini E. M., Miralda-Escudé J., Coccato L., Sarzi M., Pizzella A., Beifiori A., 2009, ApJ, 690, 537
David L. P., Jones C., Forman W., Nulsen P., Vrtilek J., O'Sullivan E., Giacintucci S., Raychaudhury S., 2009, ApJ, 705, 624
Davis J. E., 2001, ApJ, 562, 575
Di Matteo T., Quataert E., Allen S. W., Narayan R., Fabian A. C., 2000, MNRAS, 311, 507
Di Matteo T., Johnstone R. M., Allen S. W., Fabian A. C., 2001, ApJ, 550, L19
Di Matteo T., Allen S. W., Fabian A. C., Wilson A. S., Young A. J., 2003, ApJ, 582, 133
Di Matteo T., Springel V., Hernquist L., 2005, Nat, 433, 604
Donahue M., de Messières G. E., O'Connell R. W., Voit G. M., Hoffer A., McNamara B. R., Nulsen P. E. J., 2011, ApJ, 732, 40
Donato D., Sambruna R. M., Gliozzi M., 2004, ApJ, 617, 915
Done C., Gierliński M., Kubota A., 2007, A&AR, 15, 1
Dunn R. J. H., Fabian A. C., 2004, MNRAS, 355, 862
Dunn R. J. H., Fabian A. C., 2006, MNRAS, 373, 959
Dwarakanath K. S., Owen F. N., van Gorkom J. H., 1995, ApJ, 442, L1
Edge A. C., 2001, MNRAS, 328, 762
Egami E. et al., 2006, ApJ, 647, 922
Evans D. A., Worrall D. M., Hardcastle M. J., Kraft R. P., Birkinshaw M., 2006, ApJ, 642, 96
Fabbiano G., Gioia I. M., Trinchieri G., 1989, ApJ, 347, 127
Fabian A. C., Iwasawa K., 1999, MNRAS, 303, L34
Fabian A. C., Rees M. J., 1995, MNRAS, 277, L55
Fabian A. C., Hu E. M., Cowie L. L., Grindlay J., 1981, ApJ, 248, 47
Fabian A. C. et al., 2000, MNRAS, 318, L65
Fabian A. C., Sanders J. S., Allen S. W., Crawford C. S., Iwasawa K., Johnstone R. M., Schmidt R. W., Taylor G. B., 2003, MNRAS, 344, L43
Fabian A. C., Sanders J. S., Taylor G. B., Allen S. W., 2005, MNRAS, 360, L20
Fabian A. C., Sanders J. S., Taylor G. B., Allen S. W., Crawford C. S., Johnstone R. M., Iwasawa K., 2006, MNRAS, 366, 417
Fabian A. C. et al., 2011, MNRAS, 418, 2154
Falcke H., Biermann P. L., 1995, A&A, 293, 665
Falcke H., Körding E., Markoff S., 2004, A&A, 414, 895
Fender R., Belloni T., 2004, ARA&A, 42, 317
Fender R. et al., 1999, ApJ, 519, L165
Fender R. P., Belloni T. M., Gallo E., 2004, MNRAS, 355, 1105
Ferrarese L., Ford H. C., Jaffe W., 1996, ApJ, 470, 444
Finoguenov A., Jones C., 2001, ApJ, 547, L107
Finoguenov A., Ruszkowski M., Jones C., Brüggen M., Vikhlinin A., Mandel E., 2008, ApJ, 686, 911

Forman W. et al., 2005, ApJ, 635, 894
Frank J., King A., Raine D. J., 2002, Accretion Power in Astrophysics, 3rd edn. Cambridge Univ. Press, Cambridge
Freeman P. E., Kashyap V., Rosner R., Lamb D. Q., 2002, ApJS, 138, 185
Gallo E., Fender R. P., Pooley G. G., 2003, MNRAS, 344, 60
Gandhi P., Horst H., Smette A., Hönig S., Comastri A., Gilli R., Vignali C., Duschl W., 2009, A&A, 502, 457
Gebhardt K., Adams J., Richstone D., Lauer T. R., Faber S. M., Gültekin K., Murphy J., Tremaine S., 2011, ApJ, 729, 119
Gilli R., Comastri A., Hasinger G., 2007, A&A, 463, 79
Gliozzi M., Sambruna R. M., Brandt W. N., 2003, A&A, 408, 949
Graham A. W., 2007, MNRAS, 379, 711
Guainazzi M., Matt G., Perola G. C., 2005, A&A, 444, 119
Haehnelt M. G., Natarajan P., Rees M. J., 1998, MNRAS, 300, 817
Hardcastle M. J., Worrall D. M., 1999, MNRAS, 309, 969
Hardcastle M. J., Evans D. A., Croston J. H., 2006, MNRAS, 370, 1893
Hardcastle M. J., Evans D. A., Croston J. H., 2007, MNRAS, 376, 1849
Hardcastle M. J., Evans D. A., Croston J. H., 2009, MNRAS, 396, 1929
Harris D. E., Biretta J. A., Junor W., 1997, MNRAS, 284, L21
Harris D. E. et al., 2000, ApJ, 530, L81
Harris D. E., Cheung C. C., Biretta J. A., Sparks W. B., Junor W., Perlman E. S., Wilson A. S., 2006, ApJ, 640, 211
Harris D. E., Cheung C. C., Stawarz Ł., Biretta J. A., Perlman E. S., 2009, ApJ, 699, 305
Heinz S., Sunyaev R. A., 2003, MNRAS, 343, L59
Hlavacek-Larrondo J., Fabian A. C., 2011, MNRAS, 413, 313
Hlavacek-Larrondo J., Fabian A. C., Sanders J. S., Taylor G. B., 2011, MNRAS, 415, 3520
Hlavacek-Larrondo J., Fabian A. C., Edge A. C., Ebeling H., Sanders J. S., Hogan M. T., Taylor G. B., 2012, MNRAS, 421, 1360
Ho L. C., 2002, ApJ, 564, 120
Hopkins P. F., Hernquist L., Cox T. J., Di Matteo T., Robertson B., Springel V., 2006, ApJS, 163, 1
Isobe T., Feigelson E. D., 1990, BAAS, 22, 917
Isobe T., Feigelson E. D., Nelson P. I., 1986, ApJ, 306, 490
Jaffe W., McNamara B. R., 1994, ApJ, 434, 110
Johnstone R. M., Fabian A. C., Morris R. G., Taylor G. B., 2005, MNRAS, 356, 237
Kaastra J. S., 1992, in Internal SRON-Leiden Report, updated version 2.0
Kalberla P. M. W., Burton W. B., Hartmann D., Arnal E. M., Bajaja E., Morras R., Pöppel W. G. L., 2005, A&A, 440, 775
Körding E., Falcke H., Corbel S., 2006, A&A, 456, 439
Kormendy J., Gebhardt K., 2001, in Wheeler J. C., Martel H., eds, AIP Conf. Ser. Vol. 586, 20th Texas Symposium on Relativistic Astrophysics, Am. Inst. Phys., New York, p. 363
Kriss G. A., Cioffi D. F., Canizares C. R., 1983, ApJ, 272, 439
Hlavacek-Larrondo J. et al., 2013, MNRAS, in press
Lauer T. R. et al., 2007, ApJ, 662, 808
Lavalley M. P., Isobe T., Feigelson E. D., 1992, BAAS, 24, 839
Liedahl D. A., Osterheld A. L., Goldstein W. H., 1995, ApJ, 438, L115
Maccarone T. J., Gallo E., Fender R., 2003, MNRAS, 345, L19
Machacek M., Jones C., Forman W. R., Nulsen P., 2006, ApJ, 644, 155
Machacek M. E., Kraft R. P., Jones C., Forman W. R., Hardcastle M. J., 2007, ApJ, 664, 804
Machacek M. E., Jerius D., Kraft R., Forman W. R., Jones C., Randall S., Giacintucci S., Sun M., 2011, ApJ, 743, 15
Magorrian J. et al., 1998, AJ, 115, 2285
Maiolino R., Salvati M., Bassani L., Dadina M., della Ceca R., Matt G., Risaliti G., Zamorani G., 1998, A&A, 338, 781
McKinney J. C., Tchekhovskoy A., Blandford R. D., 2012, MNRAS, 423, 3083
McNamara B. R., Nulsen P. E. J., 2007, ARA&A, 45, 117
McNamara B. R., Nulsen P. E. J., 2012, New J. Phys., 14, 055023
McNamara B. R. et al., 2000, ApJ, 534, L135
McNamara B. R., Kazemzadeh F., Rafferty D. A., Bîrzan L., Nulsen P. E. J., Kirkpatrick C. C., Wise M. W., 2009, ApJ, 698, 594
McNamara B. R., Rohanizadegan M., Nulsen P. E. J., 2011, ApJ, 727, 39
Mendygral P. J., O'Neill S. M., Jones T. W., 2011, ApJ, 730, 100
Mendygral P. J., Jones T. W., Dolag K., 2012, ApJ, 750, 166
Merloni A., Heinz S., 2007, MNRAS, 381, 589
Merloni A., Heinz S., di Matteo T., 2003, MNRAS, 345, 1057
Merritt D., Ferrarese L., 2001, ApJ, 547, 140
Mewe R., Gronenschild E. H. B. M., van den Oord G. H. J., 1985, A&AS, 62, 197
Mewe R., Lemen J. R., van den Oord G. H. J., 1986, A&AS, 65, 511
Mościbrodzka M., Gammie C. F., Dolence J. C., Shiokawa H., Leung P. K., 2009, ApJ, 706, 497
Nandra K., Iwasawa K., 2007, MNRAS, 382, L1
Narayan R., Fabian A. C., 2011, MNRAS, 415, 3721
Narayan R., McClintock J. E., 2008, New Astron. Rev., 51, 733
Narayan R., Yi I., 1994, ApJ, 428, L13
Novikov I. D., Thorne K. S., 1973, in Dewitt C., Dewitt B. S., eds, Black Holes, Les Astres Occlus, p. 343
Nowak M. A., 1995, PASP, 107, 1207
O'Dea C. P. et al., 2008, ApJ, 681, 1035
O'Neill S. M., Jones T. W., 2010, ApJ, 710, 180
O'Sullivan E., Worrall D. M., Birkinshaw M., Trinchieri G., Wolter A., Zezas A., Giacintucci S., 2011a, MNRAS, 416, 2916
O'Sullivan E., Giacintucci S., David L. P., Gitti M., Vrtilek J. M., Raychaudhury S., Ponman T. J., 2011b, ApJ, 735, 11
Panessa F., Barcons X., Bassani L., Cappi M., Carrera F. J., Ho L. C., Pellegrini S., 2007, A&A, 467, 519
Paturel G., Petit C., Prugniel Ph., Theureau G., Rousseau J., Brouty M., Dubois P., Cambrésy L., 2007, A&A, 412, 45
Pellegrini S., 2005, ApJ, 624, 155
Pellegrini S., 2010, ApJ, 717, 640
Pellegrini S., Venturi T., Comastri A., Fabbiano G., Fiore F., Vignali C., Morganti R., Trinchieri G., 2003, ApJ, 585, 677
Pian E., Romano P., Maoz D., Cucchiara A., Pagani C., Parola V. L., 2010, MNRAS, 401, 677
Pizzolato F., Soker N., 2005, ApJ, 632, 821
Pizzolato F., Soker N., 2010, MNRAS, 408, 961
Plotkin R. M., Markoff S., Kelly B. C., Körding E., Anderson S. F., 2012, MNRAS, 419, 267
Poggianti B. M., 1997, A&AS, 122, 399
Proga D., Begelman M. C., 2003, ApJ, 592, 767
Ptak A., Yaqoob T., Mushotzky R., Serlemitsos P., Griffiths R., 1998, ApJ, 501, L37
Quillen A. C. et al., 2008, ApJS, 176, 39
Rafferty D. A., McNamara B. R., Nulsen P. E. J., Wise M. W., 2006, ApJ, 652, 216
Remillard R. A., McClintock J. E., 2006, ARA&A, 44, 49
Risaliti G., Maiolino R., Salvati M., 1999, ApJ, 522, 157
Rothschild R. E., Baity W. A., Marscher A. P., Wheaton W. A., 1981, ApJ, 243, L9
Russell H. R., Sanders J. S., Fabian A. C., 2008, MNRAS, 390, 1207
Russell H. R., Fabian A. C., Sanders J. S., Johnstone R. M., Blundell K. M., Brandt W. N., Crawford C. S., 2010, MNRAS, 402, 1561
Salomé P., Combes F., 2003, A&A, 412, 657
Sambruna R. M., Chartas G., Eracleous M., Mushotzky R. F., Nousek J. A., 2000, ApJ, 532, L91
Sambruna R. M., Gliozzi M., Eracleous M., Brandt W. N., Mushotzky R., 2003, ApJ, 586, L37
Sanders J. S., Fabian A. C., 2007, MNRAS, 381, 1381
Schlegel D. J., Finkbeiner D. P., Davis M., 1998, ApJ, 500, 525
Shakura N. I., Sunyaev R. A., 1973, A&A, 24, 337
Siemiginowska A., Cheung C. C., LaMassa S., Burke D. J., Aldcroft T. L., Bechtold J., Elvis M., Worrall D. M., 2005, ApJ, 632, 110
Siemiginowska A., Burke D. J., Aldcroft T. L., Worrall D. M., Allen S., Bechtold J., Clarke T., Cheung C. C., 2010, ApJ, 722, 102
Sijacki D., Springel V., 2006, MNRAS, 366, 397
Sikora M., Stawarz Ł., Lasota J.-P., 2007, ApJ, 658, 815
Silk J., Rees M. J., 1998, A&A, 331, L1
Skrutskie M. F. et al., 2006, AJ, 131, 1163
Soker N., 2008, ApJ, 684, L5
Springel V., Di Matteo T., Hernquist L., 2005, MNRAS, 361, 776

Sun M., 2009a, ApJ, 704, 1586
Sun M., 2009b, in Heinz S., Wilcots E., eds, AIP Conf. Ser. Vol. 1201, The Monster's Fiery Breath: Feedback in Galaxies, Groups and Clusters. Am. Inst. Phys., New York, p. 210
Tadhunter C., Marconi A., Axon D., Wills K., Robinson T. G., Jackson N., 2003, MNRAS, 342, 861
Taylor G. B., Sanders J. S., Fabian A. C., Allen S. W., 2006, MNRAS, 365, 705
Tchekhovskoy A., Narayan R., McKinney J. C., 2011, MNRAS, 418, L79
Terashima Y., Wilson A. S., 2003, ApJ, 583, 145
Terashima Y., Iyomoto N., Ho L. C., Ptak A. F., 2002, ApJS, 139, 1
Tremaine S. et al., 2002, ApJ, 574, 740
Vasudevan R. V., Fabian A. C., 2007, MNRAS, 381, 1235
Vestergaard M., Barthel P. D., 1993, AJ, 105, 456
Wachter K., Leach R., Kellogg E., 1979, ApJ, 230, 274
Walsh J. L., Barth A. J., Sarzi M., 2010, ApJ, 721, 762
Wu Q., Yuan F., Cao X., 2007, ApJ, 669, 96
Yi I., Boughn S. P., 1998, ApJ, 499, 198
Young M. et al., 2012, ApJ, 748, 124
Yuan F., Markoff S., Falcke H., Biermann P. L., 2002, A&A, 391, 139

This paper has been typeset from a TEX/LATEX file prepared by the author.